Forensic mapping of seismic velocity heterogeneity in a CO_2 layer at the Sleipner CO_2 storage operation, North Sea, using time-lapse seismics

R.A. Chadwick[a,*], G.A. Williams[b], I. Falcon-Suarez[c]

[a] British Geological Survey, Environmental Science Centre, Keyworth, Notts, NG12 5GG, United Kingdom
[b] British Geological Survey, The Lyell Centre, Research Avenue South, Edinburgh, EH14 4AP, United Kingdom
[c] National Oceanography Centre, University of Southampton Waterfront Campus, European Way, Southampton, SO14 3ZH, United Kingdom

ABSTRACT

CO_2 separated from natural gas produced at the Sleipner and Gudrun fields is being injected into the Utsira Sand, with around 18 million tons currently stored. Time-lapse 3D seismics have been deployed to monitor development of the CO_2 plume. The 2010 seismic survey resolved, for the first time in 3D, the topmost CO_2 layer into distinct reflections from its top and base. Seismic velocity is diagnostic of CO_2 layer properties and a forensic interpretative approach is adopted to determine spatial velocity variation in the topmost CO_2 layer. Velocity is obtained by equating absolute layer thickness, derived by subtracting a constructed flat CO_2 – water contact from the topographical relief of the reservoir top, to the temporal separation of the layer top and base reflections, with appropriate correction for wavelet interference effects. Layer velocities show a systematic and robust spatial variation between a northern area with a mean velocity of $1371 \pm 122 \, \text{ms}^{-1}$ and a central area with a much higher mean velocity of $1638 \pm 103 \, \text{ms}^{-1}$. Recent fluid flow simulations of the topmost CO_2 layer have shown that incorporating a high permeability channel in the model reservoir significantly improves the history-match. This high permeability channel corresponds remarkably closely to the low seismic velocities mapped in the northern area, with higher layer velocities of the central area interpreted as more argillaceous, less permeable overbank deposits. The new velocity analysis therefore provides independent support for including deterministic permeability heterogeneity in predictive fluid flow modelling of Sleipner.

1. Introduction

1.1. Injection and geology

Large-scale underground storage of anthropogenic carbon-dioxide is a key technology for keeping cumulative man-made emissions of greenhouse gases within safe limits (IPCC, 2005; ETI, 2015). Indeed, it is a key element in negative emissions technologies such as bio-energy with CCS (BECCS) and direct air capture and storage of CO_2 (DACCS) (CCC, 2019). The CO_2 injection operation at Sleipner in the Norwegian central North Sea commenced in 1996 and is the world's longest-running industrial-scale storage project (Baklid et al., 1996).

CO_2 separated from natural gas produced at the Sleipner Vest field, and since 2014 the Gudrun field, is being injected into the Utsira Sand, a regional saline aquifer of late Cenozoic age (Fig. 1a). The Utsira Sand is interpreted to have been deposited within a narrow north-trending, elongate, shallow seaway, with current directions dominantly north-south, either as sandy shelf shoals (Galloway, 2002) or a submarine fan system (Gregersen and Michelsen, 1997). Mud diapirism in underlying strata during deposition of the sand produced north-trending depositional fairways which are likely to have formed preferential loci for channel systems (Williams and Chadwick, 2017). The aquifer is in excess of 200 m thick at Sleipner and comprises mostly clean unconsolidated sand of high porosity (> 0.3) and permeability (> 1 darcy). A number of thin intra-reservoir mudstones, typically 1–2 m thick, are evident from geophysical logging in wells around Sleipner (Fig. 1b).

The CO_2 is injected in a dense phase via a deviated well at a depth of 1012 m below sea level, some 200 m beneath the reservoir top. Injection commenced in 1996, at a roughly constant rate of 0.8 to 0.9 million tons per year, with around 17 million tons of CO_2 stored by the end of 2017 (Eiken, 2019).

1.2. Time-lapse monitoring

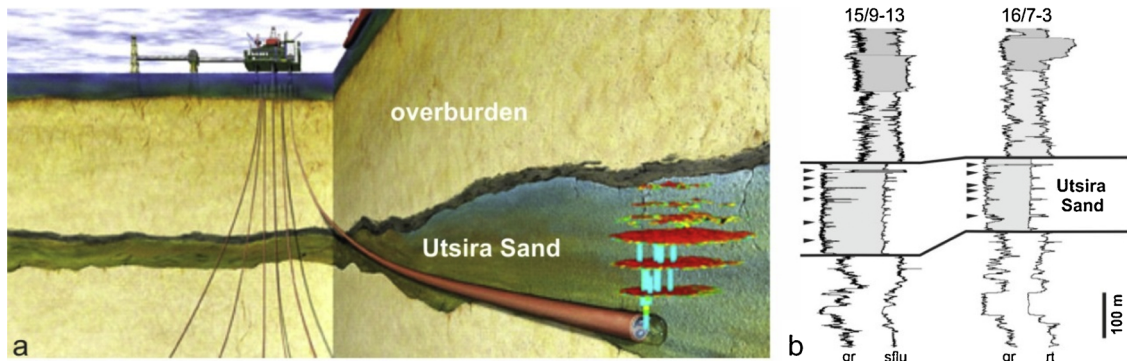A deep-focused non-invasive monitoring programme has been

---

Fig. 1. a) Schematic representation of the Sleipner CO_2 injection operation. b) Sample geophysical logs through the Utsira Sand from two wells in the Sleipner area. Note the low γ-ray signature of the Utsira Sand, with peaks corresponding to the intra-reservoir mudstones. gr = γ-ray log, sflu/rt = resistivity logs. Sleipner schematic courtesy of Equinor ASA.

deployed at Sleipner, with time-lapse seismic proving to be the key tool (Arts et al., 2008). A baseline 3D survey was acquired in 1994, with repeat surveys in 1999, 2001, 2004, 2006, 2008, 2010, 2013 and 2016. Surveys up to 2010 are now publicly available (Eiken, 2019). A key objective is to quantitatively verify or constrain predictive flow simulations of plume development to demonstrate understanding of reservoir processes and provide the basis for predicting future plume behaviour. However, because the injection well is near-horizontal, no wellbore penetrates either the CO_2 plume or the exact stratigraphy that the plume now occupies, and quantitative analysis is challenging.

The plume is imaged on the seismic data as a tiered structure some 200 m high comprising a number of bright sub-horizontal reflections (Fig. 2). These are interpreted to arise from thin layers of CO_2 trapped beneath the intra-reservoir mudstones which are partially but not wholly sealing. The reflective layering had formed by 1999 with each individual reflection traceable on all subsequent surveys. A prominent vertical 'chimney' feature lies above the injection point and is interpreted as the main conduit for upward migration of CO_2 through the reservoir and the main feeder of the layers. Reflections from the middle and upper plume have generally increased in amplitude and lateral extent on successive time-lapse surveys, whereas the lower plume reflections have ceased growing, in some cases shrinking and dimming (Boait et al., 2012).

1.2.1. CO_2 layer velocities

Crucial to understanding the migration and development of the CO_2 layers are their geophysical and physical properties. Seismic velocity is a key diagnostic parameter in this respect and can be estimated from rock physics, but there is significant uncertainty in this approach. Parameter estimation at Sleipner relies on data from scattered well logs or from a single core, and none of the data are from the location of the plume itself, which is not penetrated by any wellbore. At Sleipner therefore, 'average' reservoir properties or values from single core measurements have traditionally been used in rock physics velocity determination (Arts et al., 2004a, 2004b). Properties of the injected

CO_2 are also somewhat uncertain in terms of the exact pressure-temperature conditions at various depths in the plume (Alnes et al., 2011) and also the concentration of methane impurity, nominally 1–2% in the injection stream.

In order to derive maximum information on layer properties, direct measurement of velocity from the seismic data itself is a key aspiration, and particularly the ability to map any spatial velocity variation that might be present. Seismic inversion can provide direct estimates of acoustic impedance (e.g. Clochard et al., 2010; Delépine et al., 2011) but because of resolution limitations, tuning effects, and parameter uncertainty, accurate derivation of layer velocity is very challenging, particularly in 3D. This is exemplified by inversion results to date. Queißer and Singh (2013a, 2013b) used full waveform inversion (FWI) on a 2D line, and related the velocity changes to CO_2 saturation using a rock physics model. Raknes et al. (2015) carried out 3-D elastic FWI on the plume but found the problem to be non-linear, ill-posed and very sensitive to parameter assumptions. Ghosh et al. (2015) inverted post-stack data for CO_2 saturation, and found large uncertainties attached to the rock physics assumptions.

This paper utilises a detailed integrated 'forensic' interpretative approach to provide additional quantitative constraints on layer velocities.

1.3. Topmost layer history matching

It is expected that, with time, most of the injected CO_2 will end up in the topmost layer, trapped beneath the undulating reservoir topseal where it has the potential to migrate laterally over significant distances (Chadwick et al., 2004). How this layer develops through time is therefore crucial to understanding and predicting medium and longer-term storage site performance and has been the subject of much recent research.

Reflection amplitude changes at the top of the Utsira Sand illustrate the progressive growth of the topmost layer through time (Fig. 3). A north-trending linear prolongation of the layer is particularly
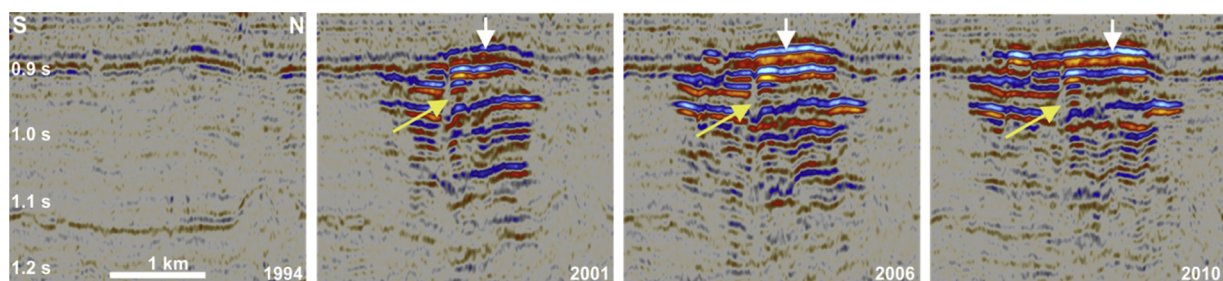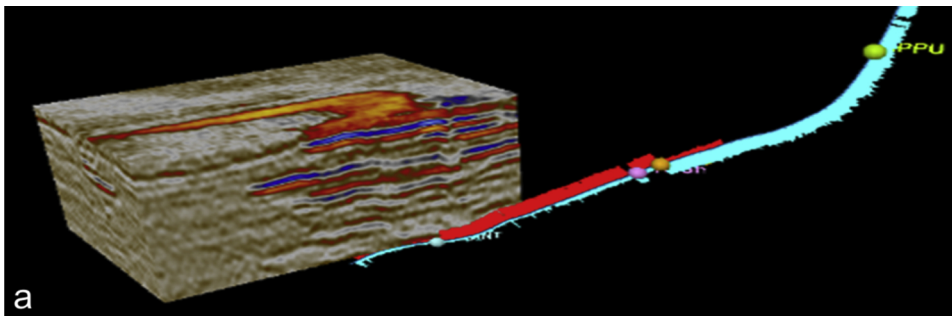

Fig. 2. Development of reflectivity on a N–S seismic inline from the Sleipner CO_2 plume showing its evolution from 1994 (baseline) to 2010 (time-lapse processing). White arrow denotes topmost CO_2 layer. Yellow arrow indicates main plume feeder chimney. Note opposite display polarity to subsequent figures.

Fig. 3. a) 3D view of part of the 2006 seismic cube showing the deviated injection wellbore, the reflective plume and the geometry of the topmost CO_2 layer. b) Reflection amplitude difference maps of the topmost layer in 2001, 2006 and 2010, showing its development with time. Faint black polygons show extent of the whole plume and the white disc denotes the location of the principal feeder chimney.
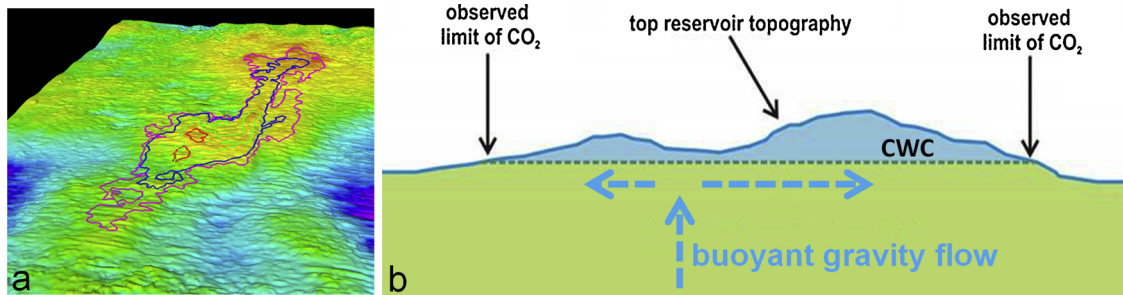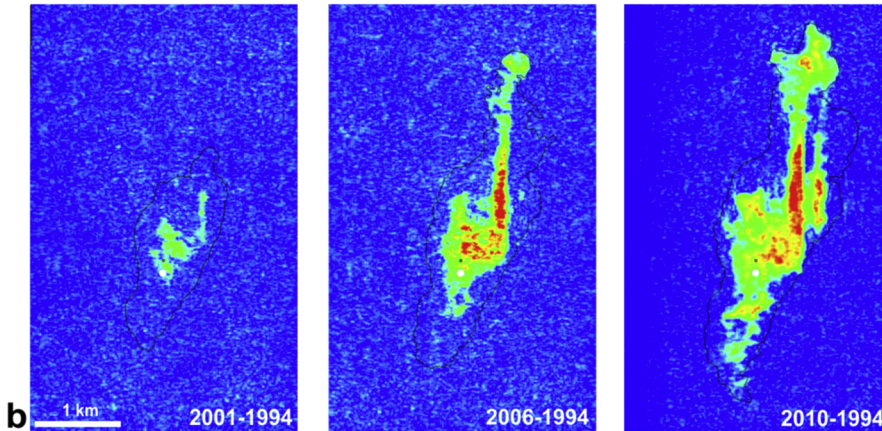
Fig. 4. Topseal topographical controls on growth of the topmost CO_2 layer. a) Perspective view of the top reservoir surface showing layer extents in 1999 (red), 2001 (green), 2006 (blue) and 2010 (purple). b) Schematic section showing CO_2 layer spreading by buoyant infill of topseal relief, above a flat CO_2 – water contact (CWC).

prominent and corresponds to CO_2 migrating northwards beneath a linear ridge in the reservoir topseal (Fig. 4a), which formed by differential compaction above an underlying channel (Williams and Chadwick, 2017). A similar ridge lies to the east, filling from 2006 onwards and prominent on the 2010 data. The overall positive relief of the domes and ridges compared to the surrounds is typically up to around 20 m, corresponding to about 20 ms two-way travel-time (TWTT). A robust understanding of layer morphology requires an accurate knowledge of the small topographic depth changes around the structural features that it occupies, but in principle it is possible to derive the thickness of the CO_2 layer by knowing its lateral extents and the top reservoir (base topseal) topography (Section 4.3).

The way the shape of the topmost layer corresponds closely to the structural relief of the reservoir top suggests that it is spreading by a dominantly buoyancy-driven fill-spill process, with CO_2 supplied from the deeper plume migrating laterally beneath the topseal relief (Fig. 4b) and above a flat CO_2 – water contact (CWC).

A number of numerical flow simulations of the growth of this CO_2 layer have been published, but all have come up against the same issue - a difficulty in replicating the very rapid northward migration of CO_2 along the linear ridge (e.g. Chadwick and Noy, 2010; Zhu et al., 2015). Various controlling parameters in the modelling have been

investigated, including small uncertainties in topseal topography, azimuthal permeability anisotropy, CO_2 composition and reservoir temperature (Chadwick and Noy, 2010; Zhu et al., 2015). Alternative modelling approaches have also been tried, including vertical equilibrium solutions and models with non-darcy flow such as invasion percolation (Cavanagh, 2013; Cavanagh and Haszeldine, 2014). A key element of all these models is that they have assumed an essentially homogeneous reservoir sand, albeit with a degree of permeability anisotropy in some cases (Chadwick and Noy, 2010; Zhu et al., 2015).

1.4. Channel related permeability heterogeneity in the reservoir

Recent re-appraisal of the baseline seismic and geophysical log data has led to significant progress in understanding the permeability structure of the topmost sand body. From the baseline seismic data, Williams and Chadwick (2017) mapped a north-trending channel in the topmost sand which corresponds to the north-trending ridge in the topseal surface. On the basis of geophysical logs from the vicinity they further conjectured that the channel-fill might be higher permeability than the single existing core of Utsira Sand which was not obtained from a channel area. Incorporating this channel into the flow models as a high permeability feature has greatly improved the history-match of

the topmost layer from numerical darcy-flow modelling (Williams and Chadwick, 2017; Cowton et al., 2018). Nevertheless, the assumption of higher permeability does remain conjectural and additional independent evidence is important to verify the hypothesis.

1.5. Aims of this paper

The primary aim of this paper is to use a forensic interpretive analysis to determine seismic velocity in the topmost CO_2 layer at Sleipner and to detect and map any lateral velocity variations that might be present. Channelling is clearly very important in controlling the way that the CO_2 layer has developed through time and an additional aim of the paper is to investigate whether detailed evaluation of seismic velocity in the layer can provide independent evidence for the presence of channelling and lateral permeability variation.

2. Rock physics constraints on CO_2 layer seismic velocity

2.1. Introduction

Until recently, no experimental reservoir rock physics data were available from Sleipner, and velocity determination depended on modelling well log data from water-saturated Utsira Sand with assumed CO_2 fluid properties. The temperature at the top of the reservoir is about 29C (Alnes et al., 2011) with pressure likely close to hydrostatic (Chadwick et al., 2012). Equations-of-state and experimental data for CO_2 all agree that at these conditions CO_2 is in a dense phase with a density around 50–70% that of water and a compressibility less than 5% that of water, the latter resulting in its low seismic velocity. Arts et al. (2004a, 2004b) using Gassman fluid substitution, concluded that seismic velocities in the CO_2 layers are reduced from about $2050\,ms^{-1}$ in the water-saturated sand to around 1400 to $1500\,ms^{-1}$, for their median estimate of CO_2 properties. Arts et al. (2004a, 2004b) assumed uniform (homogeneous) fluid mixing at seismic wavelength scales, with the implication that these velocity estimates would apply to a wide range of CO_2 saturations (greater than about 0.2).

2.2. New laboratory data

Obtaining reliable laboratory measurements from unconsolidated sand samples is notoriously difficult, but recently Falcon-Suarez et al. (2018) have reported a suite of geophysical measurements from an Utsira Sand core sample (Fig. 5). The full experimental methodology is described in Falcon-Suarez et al. (2018); suffice to say here that

simultaneous ultrasonic and electrical resistivity tomography measurements were obtained at reservoir conditions, the latter for mapping S_{CO2} in the sample from the Archie formula. Readings were obtained for a range of CO_2 saturations, pore pressure and effective stress. A significant aspect of these measurements is that the experiments tracked up and back through multiple pressure and CO_2 saturation cycles with notably repeatable results being obtained.

Using the fully water-saturated measurements, readings of Vp were adjusted to an effective stress of 6.17 MPa; in line with conditions at the top of the Utsira reservoir. It is likely that CO_2 fluid properties varied slightly over the range of pore-pressures investigated in the experiment, but above the Critical Point these would be minor.

Measured velocities range from around $2050\,ms^{-1}$ in the fully water-saturated sand (in line with borehole log measurements from the vicinity) to minimum values of around $1450\,ms^{-1}$ at CO_2 saturations between 0.2 and 0.4. No CO_2 saturations above 0.4 were obtained. This might reflect limitations of the core-flooding methodology and/or more fundamental residual water limits in this particular sample.

Velocity-saturation relationships were then calculated with a Gassmann/Brie model from the water-saturated properties of the core sample (Falcon-Suarez et al., 2018) using fluid substitution with CO_2 properties matched to top reservoir conditions. These indicate velocities of around $1400\,ms^{-1}$ at higher CO_2 saturations. Reduced velocity decrease at lower CO_2 saturations is consistent with a Brie exponent of around e = 5. This is conventionally interpreted as indicative of a strong element of 'semi-patchy' mixing between the two fluids in the sample, operative at the ultrasonic frequencies of the experiment. However recent theoretical work by Papageorgiou et al. (2016) and Papageorgiou and Chapman (2017) indicates that this type of velocity-saturation relationship does not necessarily require 'patchy' fluid mixing, but can arise purely from capillary pressure effects between the two fluid phases. Importantly, this effect is independent of frequency and so velocity measurements from ultrasonic experiments could also be applicable to seismic frequencies. With the proviso that porosity characteristics at the core scale are representative of the larger scale, the core measurements should therefore provide useful new constraints on velocities in the Sleipner CO_2 plume.

2.3. Possibilities for lateral velocity variation

The liklihood of property heterogeneity in the Utsira Sand is supported by borehole geophysical logs. These show ample evidence of velocity variation (Fig. 6), though, because they sample a rather restricted set of point locations in the very laterally extensive reservoir,
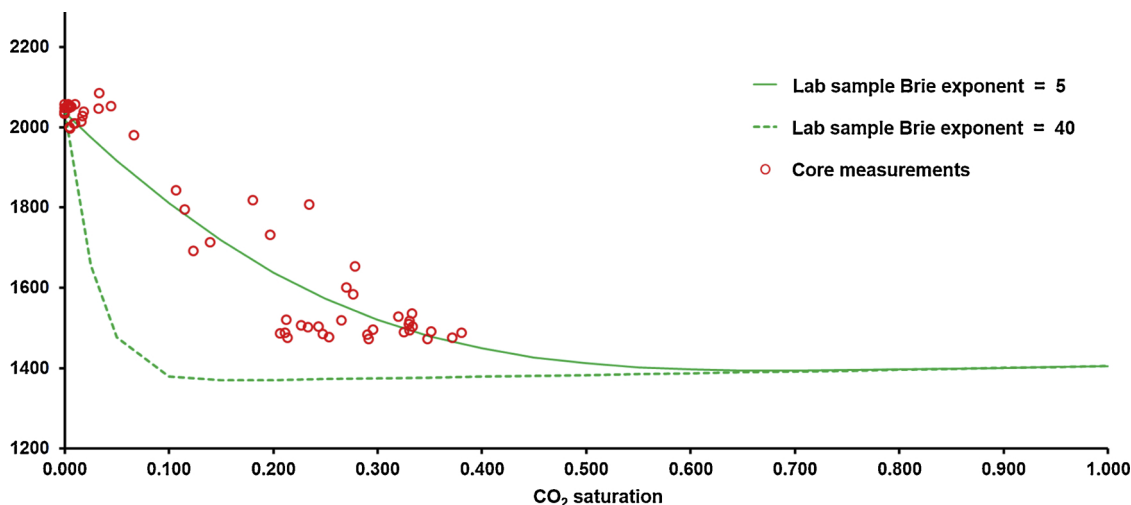
Fig. 5. Vp − CO_2 saturation relationships for the analysed core sample from the Utsira Sand, showing adjusted laboratory measurements and calculated values for two Brie models.
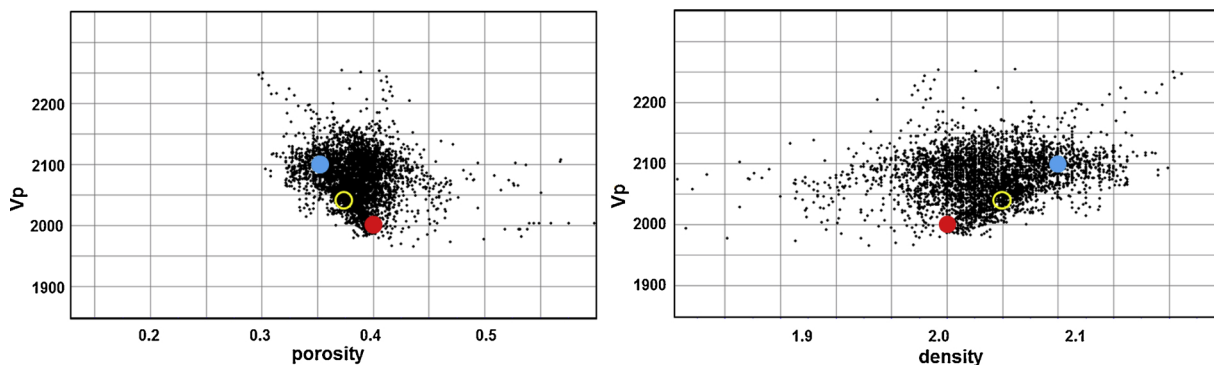
Fig. 6. Cross-plots of velocity against porosity and density from well logs in the Utsira Sand. The 'Fast Sand', 'Slow Sand' and laboratory core sample are denoted by the blue, red and open discs respectively.

not necessarily the whole velocity range.

In order to examine the possible effect of this variation on CO_2 layer velocity we arbitrarily define two notional types of reservoir sand, 'Fast' and 'Slow', with velocities of 2100 and 2000 ms^{-1}, porosities of 0.35 and 0.4 and densities of 2.1 and 2.0 gcm^{-3} respectively (Fig. 6). We postulate that the 'Slow' sands, with higher porosity, might correspond with the higher permeability channel features discussed above. Conversely, 'Fast' sands with lower porosity might correspond to inter-channel deposits. The laboratory core sample has properties that are intermediate between those of the 'Fast' and 'Slow' sands.

Using these parameters, velocity-saturation relationships for the 'Fast' and 'Slow' sands were calculated by a Gassmann/Brie model with a Brie exponent of 5 and CO_2 properties matched to top reservoir conditions (Fig. 7). The effect of sand type on CO_2 layer velocity is clear: at high CO_2 saturations velocities can range from less than 1400 ms^{-1} for 'Slow' sands to more than 1500 ms^{-1} for 'Fast' sands. At low-intermediate CO_2 saturations velocities are typically around 1500 ms^{-1} for the 'Slow' sands and 1600 ms^{-1} for the 'Fast' sands.

So, by combining rock physics, well log data and laboratory measurements we can predict that CO_2 layer velocities in the Sleipner plume are likely to show significant variation depending both on the type (depositional facies) of sand and the fluid saturation.

3. Mapping seismic velocity structure in the topmost CO_2 Layer

3.1. Thin layer interference and tuning

It was quickly recognised (e.g. Arts et al., 2004a, 2004b) that CO_2 plume reflectivity at Sleipner was strongly influenced by thin-layer interference and tuning affects, particularly in the case of the early repeat surveys when the CO_2 layers were largely below the tuning thickness (one quarter of the dominant seismic wavelength). General aspects of thin-layer interference, particularly its effect on reflection amplitude are well understood (e.g. Widess, 1973), allowing reflection amplitudes at Sleipner to be used for the estimation of layer thickness and for plume quantification (e.g. Arts et al., 2004a, 2004b; Chadwick et al., 2004, 2005; Kiær, 2015). More subtle interference effects, notably those which involve small time-shifts of the wavelet trough and peak, are perhaps less well documented (e.g. Kallweit and Wood, 1982), but are a key focus of this paper. Cowton et al. (2016), convolved a zero-phase Ricker wavelet with spike reflection co-efficients to produce the interfering reflections, and set out very clearly the way in which layer temporal thickness induces small time-shifts of the top and base layer reflections. This is illustrated by a wedge of low-velocity material thickening from zero to well beyond the tuning thickness (Fig. 8).

Below the tuning thickness the wavelet is characterised by constant temporal spacing between the reflection 'trough' from the layer top and the reflection 'peak' from the layer base (Fig. 8). This is here termed the 'stable sub-tuning spacing'. It is larger than the true temporal thickness (which decreases to zero at the layer edge), and for the Sleipner 2010
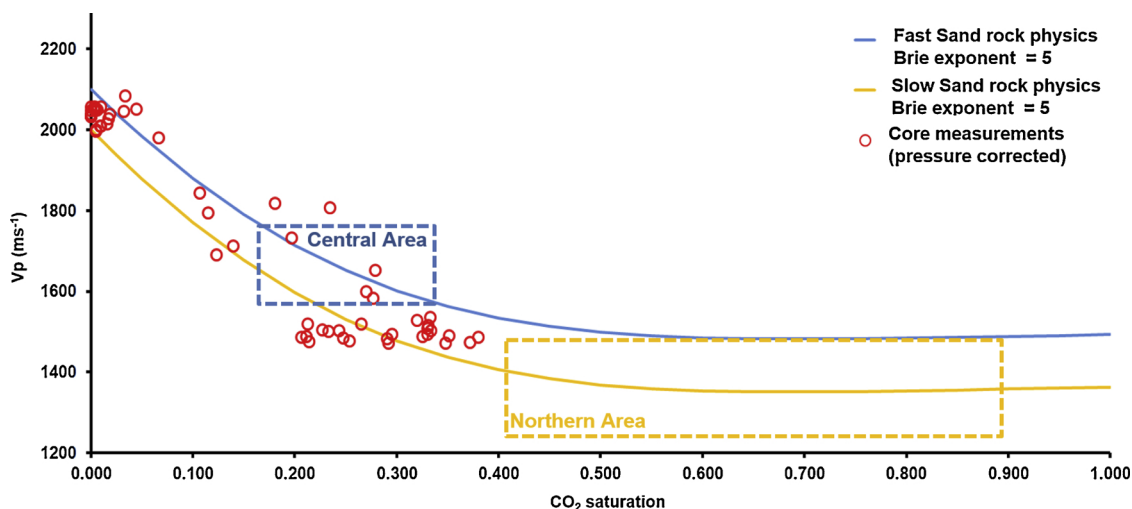

Fig. 7. Vp − CO_2 saturation relationships for the 'Fast' and 'Slow' sands (Brie parameter e = 5), together with the adjusted laboratory measurements. Dashed rectangles delineate the extracted observed velocity ranges from the Northern and Central Areas and the inferred CO_2 saturations (see Discussion).
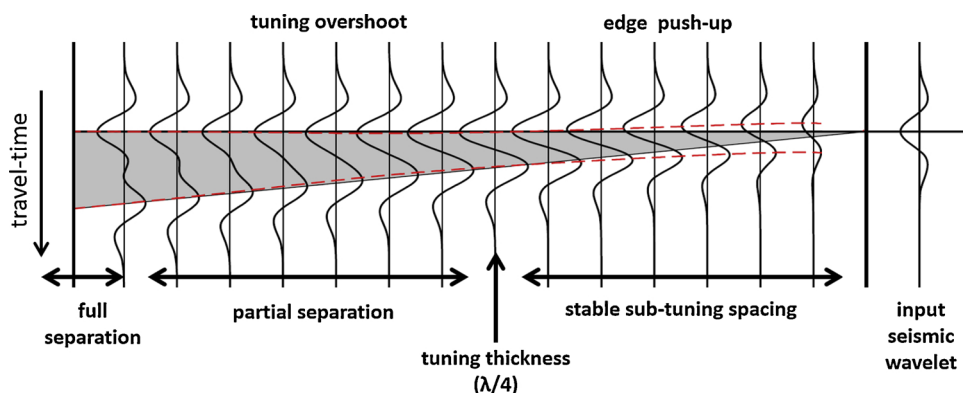
Fig. 8. Schematic synthetic seismic section through a low velocity wedge (in grey) showing wavelet interference effects from the edge to above the tuning thickness. The dashed red lines denote picks on the top layer reflection trough and the base layer reflection peak, their separation denoting the observed temporal spacing. Adapted from Cowton et al., 2016.

data has a value of around 6 ms (see below). At the tuning thickness the observed temporal spacing exactly matches the true temporal thickness. Above the tuning thickness the observed temporal spacing starts to increase gradually through a 'partially separated' stage where it is slightly less than the true temporal thickness. As the layer thickens further a point is reached where interference effects become minimal and the observed temporal spacing of the top and base reflections matches the true temporal spacing of the layer, with the top and base reflections 'fully separated'.

'Edge push-up' arises for thin layers well-below the tuning thickness - as the layer thins towards zero the sub-tuning wavelet sits progressively more symmetrically about the layer, resulting in the top reflection trough being displaced above the top layer datum (Fig. 8). This was first described at Sleipner by Arts et al. (2004a, 2004b), was subsequently used by Furre et al. (2015) to estimate the age of emplacement of the CO_2 layers and then by Cowton et al. (2016) and White et al. (2018) to estimate the true temporal thickness of very thin layers. 'Tuning overshoot' affects the partially-separated wavelet and arises from slightly differing rates of amplitude decline on the main lobe and the side-lobe as they move away from exact temporal alignment at the tuning thickness. This effect has not been remarked upon at Sleipner previously, but it requires correcting when estimating the true temporal thickness from the observed temporal spacing. These effects are examined further in the synthetic seismic modelling (Section 4).

The 2010 seismic survey, for the first time on the 3D data, achieved partial separation of the top and base layer reflections from the topmost CO_2 layer (Furre et al., 2015). This has enabled a novel method for velocity determination over the thicker parts of the topmost CO_2 layer that uses an interpreted position of the CO_2-water contact to calculate the true CO_2 layer thickness and correlates this with the temporal thickness of the layer (Chadwick et al., 2016). Initial analysis by Chadwick et al. (2016) over a restricted part of the layer yielded velocities of around $1400 \pm 100\,\mathrm{ms}^{-1}$. Here we modify the methodology and include corrections for edge push-up and tuning overshoot to provide a more detailed and spatially extensive assessment of layer velocity, including lateral velocity variation.

3.2. High-resolution 3D seismic survey in 2010

The 3D survey at Sleipner acquired in 2010 had a novel streamer configuration utilising dual sensor streamer technology which combines hydrophone recording with vertical particle movement recording to allow separation of the upgoing and downgoing wavefields. This helps to eliminate the receiver ghost and gives broader frequency content than hydrophone data alone (Furre and Eiken, 2014). Thus, the conventional time-lapse data at Sleipner have typically had a frequency spectrum in the range 8–80 Hz (-20 dB), whereas the 2010 data span the range 8–110 Hz (-20 dB). The migrated data are available in a number of offset ranges (Fig. 9). The full-offset data generally have the best signal-to-noise ratio and better rejection of multiples, but the near-

offset data show superior spatial and temporal resolution of individual reflections and are used for all of the analysis described below.

Images of the topmost layer reflections on the 2010 dataset clearly show the transition from a sub-tuning wavelet near the layer edges to partially separated reflections in the layer centre (Fig. 9a). This is shown even more strikingly on a west-east section (Fig. 9b) through north-trending ridges in the topseal (Fig. 10a), with partial separation beneath the ridges and stable sub-tuning spacing elsewhere. The spatial distributions of the sub-tuning wavelet and the partially separated reflections are clearly displayed by mapping the observed temporal spacings (Fig. 10b), the more peripheral parts of the layer being characterised by sub-tuning spacings, whereas reflections from the central parts show partial separation. A histogram of the temporal spacings (Fig. 10c) shows a skewed distribution comprising two components: sub-tuning spacings (schematically in yellow) ranging from around 5 to 7 ms with a sharply-defined modal peak of 6 ms and partially separated reflections (schematically in green) with a range of larger spacings up to 15 ms. The variation, or 'jitter', particularly evident in the sub-tuning spacings, results principally from seismic noise which has the effect of shifting the wavelet peaks slightly from trace to trace and also discretisation effects within the interpolated waveform as interpreted on the workstation. It is clear that the larger temporal spacings correspond very closely with topographic highs in the topseal relief (Fig. 10a), as would be expected given the bouyancy-driven infill process driving the layer growth (Fig. 4). Local elevation differentials between the ridge / dome features and intervening lower areas are typically up to around 15 m or more.

In detail, the layer reflectivity shows some interesting features, particularly evident in the vicinity of the two north-trending linear ridges (Fig. 9b). The reflection from the layer top follows the topseal relief and shows the two ridges clearly. Although the base of the CO_2 layer (the CO_2 – water contact) is expected to be roughly flat in depth (Fig. 4b), the base reflection geometry is more complex in two-way travel-time. The westerly ridge shows partial separation of the top and base reflections, with a pronounced velocity pushdown of the latter, whereas the easterly ridge shows partial separation, but an essentially flat (in travel-time) base reflection. Further along the easterly ridge the basal reflection actually rises slightly beneath the ridge, with an apparent 'velocity pull-up'.

In qualitative terms these differing reflection geometries can be explained in terms of differing CO_2 layer thickness beneath the ridges and are examined further via synthetic seismic modelling in the next section.

4. Synthetic seismic models

4.1. Ridge model

In order to investigate these observations in more detail and to quantify the edge-push-up and tuning overshoot effects, an extensive
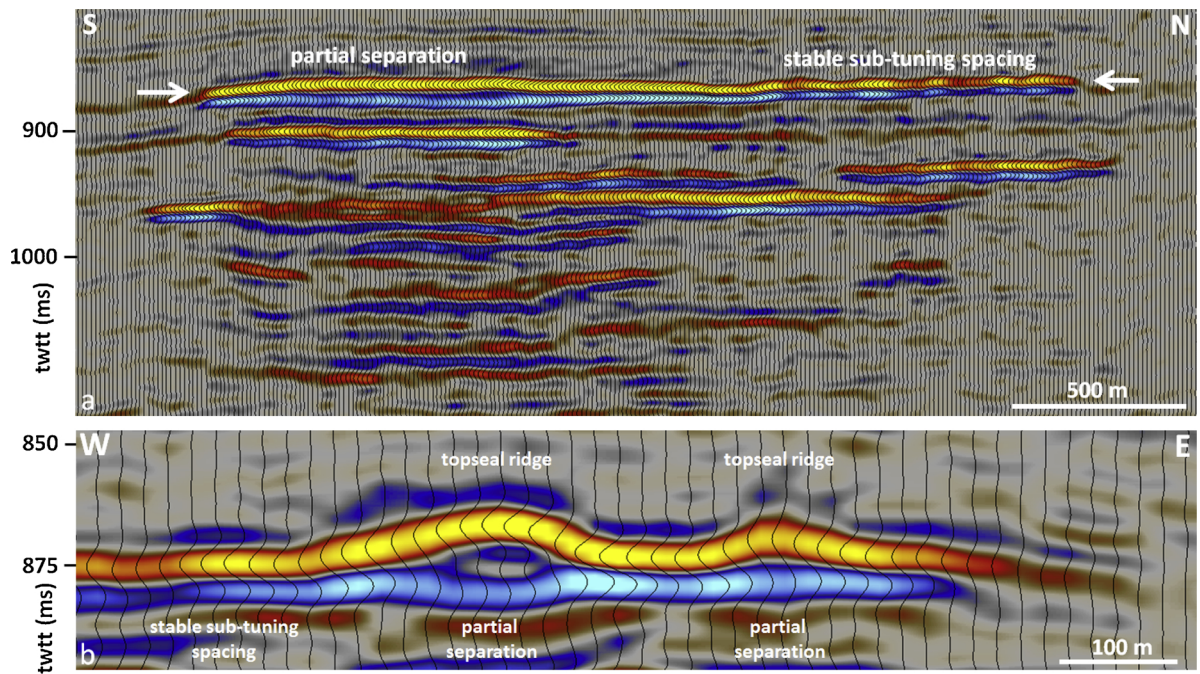
Fig. 9. a) North-south seismic line (full-offset data) through the 2010 plume with topmost CO_2 layer reflections (arrowed) showing partial separation in southern part. b) West-east seismic line (near-offset data) showing topmost CO_2 layer with top and base reflections showing partial separation beneath topseal ridges and stable sub-tuning spacing elsewhere. Line locations given in Fig. 10a.

synthetic seismic modelling exercise was carried out. This was based around a 3D model comprising an overburden overlying a flat-topped sand-filled ridge 10 m high with sloping flanks, characteristic of the topseal topographic relief infilled by the topmost CO_2 layer. The ridge contains a variable thickness of CO_2, ranging from zero at one end and

thickening along the ridge axis, via 1 m increments, to a fully-filled ridge with 10 m of CO_2 at the other end (Fig. 11).

Model properties (Table 1) were based on log data from surrounding boreholes (Fig. 6) and seismic stacking velocities (see below), and rock physics for the CO_2-saturated layer (Fig. 7). Note that although the CO_2
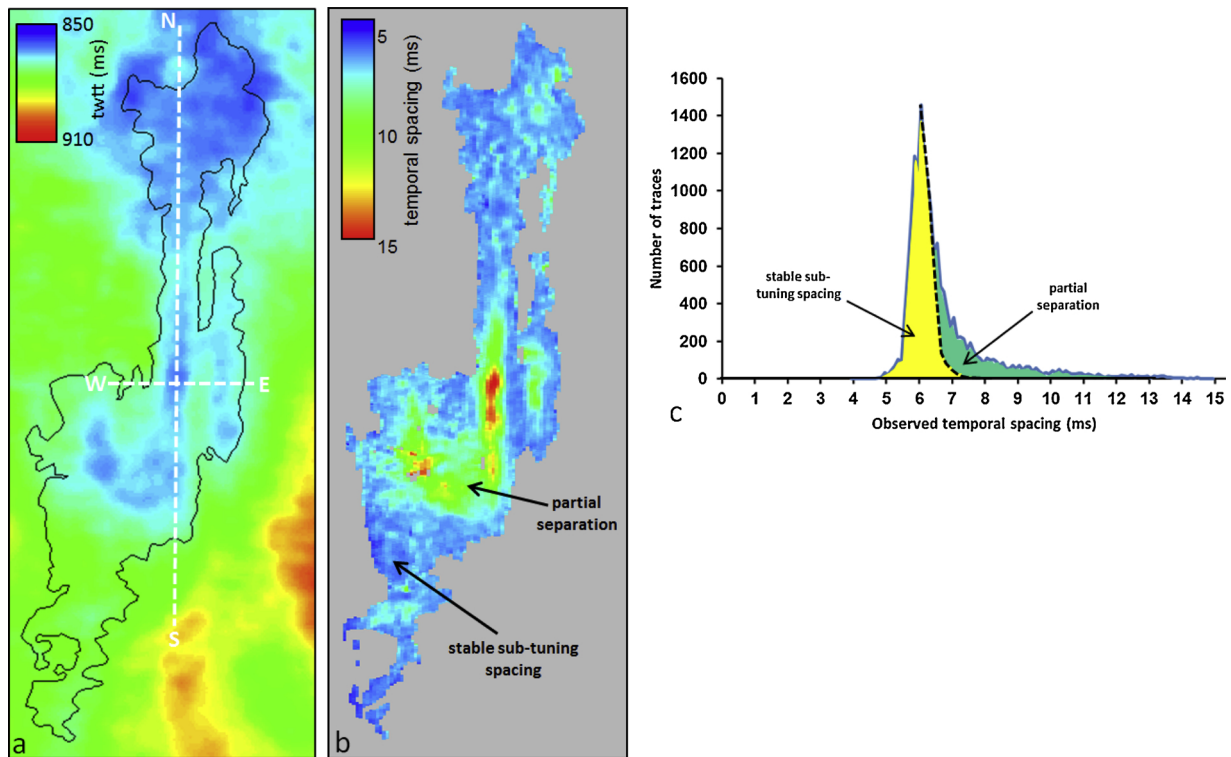

Fig. 10. a) Two-way travel-time map of the top Utsira Sand (base topseal) topography, showing the domal structures and ridges. b) Map of measured temporal spacing of the topmost CO_2 layer reflections (near offset 2010 data). c) Histogram showing the distribution of observed temporal spacings (near offset data) on all seismic traces within the layer extents. Black polygon shows outer limit of the topmost CO_2 layer. White dashes show locations of seismic lines in Fig. 9.
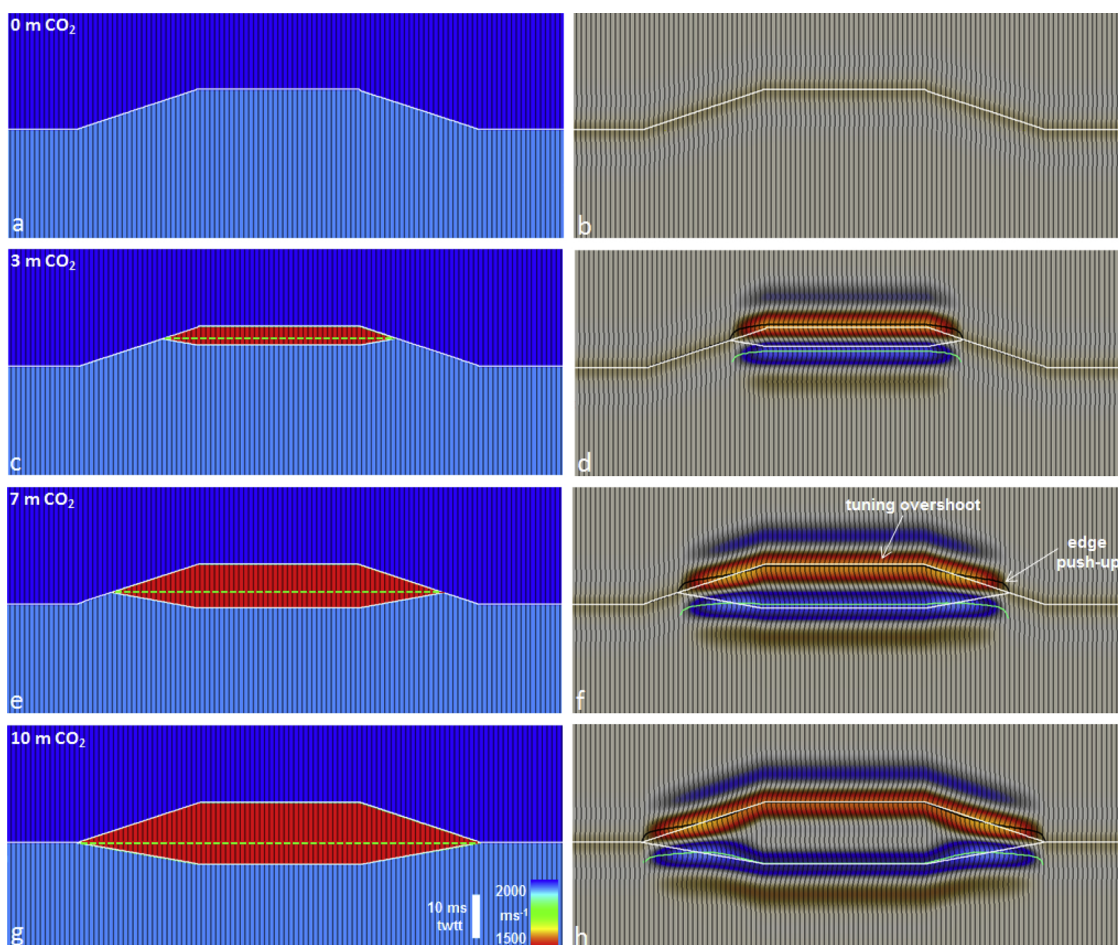
Fig. 11. Selected transects through the ridge model showing velocity (left) and corresponding synthetic seismic sections (right). All sections are in two-way travel-time (TWTT) with orange reflections denoting a negative impedance contrast and blue positive. White lines denote interfaces on the velocity model. Black and green solid lines denote picks on the top and the base of the CO_2 layer respectively. Dotted green line on the velocity sections denotes the notional position (without velocity pushdown) of the flat CO_2 – water contact (CWC).

Table 1
Physical properties of the synthetic model.

	Vp (ms^{-1})	Density (kg m^{-3})
Overburden (mudstone)	2150	2150
Reservoir sand (water - saturated)	2050	2050
Reservoir sand (CO_2 - saturated)	1400	1920
Seismic wavelet	57 Hz Ricker	

–water contact (CWC) is perfectly flat in depth, in two-way travel-time it dips down beneath the ridge flanks because of velocity pushdown (Fig. 11a,c,e,g).

4.2. Seismic wavelet

In order to generate accurate synthetic seismic data, it is important to determine as precisely as possible the shape of the seismic wavelet as it impinged on the topmost CO_2 layer. Here we are particularly interested in temporal interference effects and so a key requirement of the wavelet is that it produces the observed stable sub-tuning temporal spacing of ~6 ms (see above).

A wavelet was extracted from the seismic data (Fig. 12a), avoiding the strong tuned reflections of the CO_2 plume itself, according to the procedure below:

1) 56,000 seismic traces outside the plume footprint were selected for analysis from the 2010 high resolution near-offset survey (Fig. 12a).
2) Traces were extracted in a 256 ms window about a seismic pick in the uppermost part of the Utsira Sand (the '5 m Mudstone').
3) Auto-correlation functions were generated for the windowed traces and an average computed.
4) Tapers were applied to the average autocorrelation function using different window functions.

The wavelets with various tapers were assessed with respect to matching the frequency spectrum of the observed near-offset data and producing a stable ~6 ms sub-tuning temporal spacing, and a preferred wavelet chosen (Fig. 12b, c)

A Ricker pulse was generated for comparison, with a peak frequency of 57.5 Hz, matching the observed mean trough-to-side-lobe spacing of 6.8 ms (Fig. 12b, c), and producing a stable sub-tuning spacing of 6.1 ms. Synthetic modelling of side-lobe amplitudes on the observed top CO_2 reflection and of observed seismic data from well-logs at nearby well N15/9–13 gave very similar results with both the extracted and the 57.5 Hz Ricker wavelets. For reasons of computational efficiency therefore, the Ricker wavelet was used for the synthetic modelling described below.

4.3. Synthetic seismic results

Synthetic seismic data were generated from the velocity model and the wavelet via a 1-D finite difference code (Fig. 11b,d,f,h). Selected
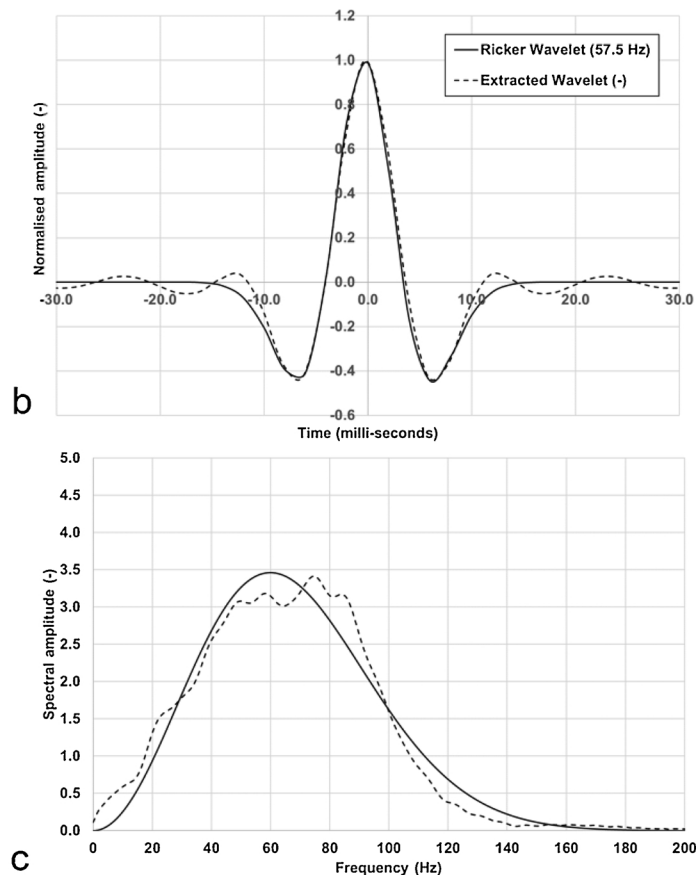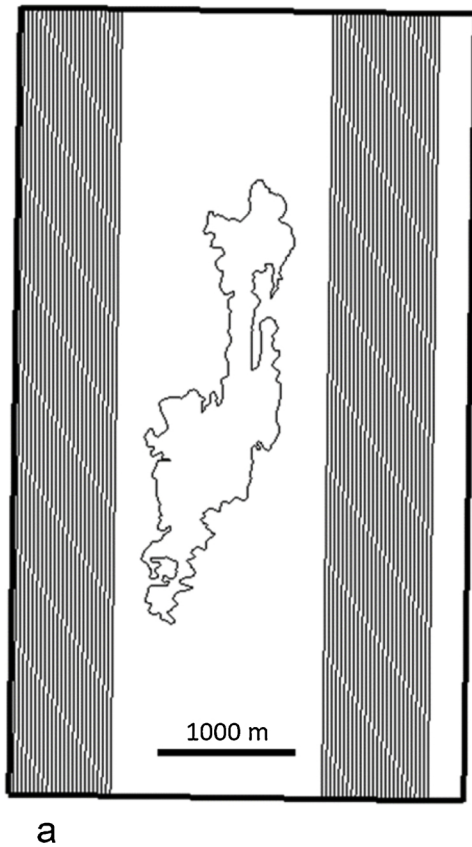
Fig. 12. a) Map showing the traces (in grey), east and west of the CO_2 plume, from which the wavelet was extracted (polygon denotes outline of topmost CO_2 layer reflectivity). b) Extracted and Ricker wavelets. c) Frequency spectra of the extracted and Ricker wavelets.
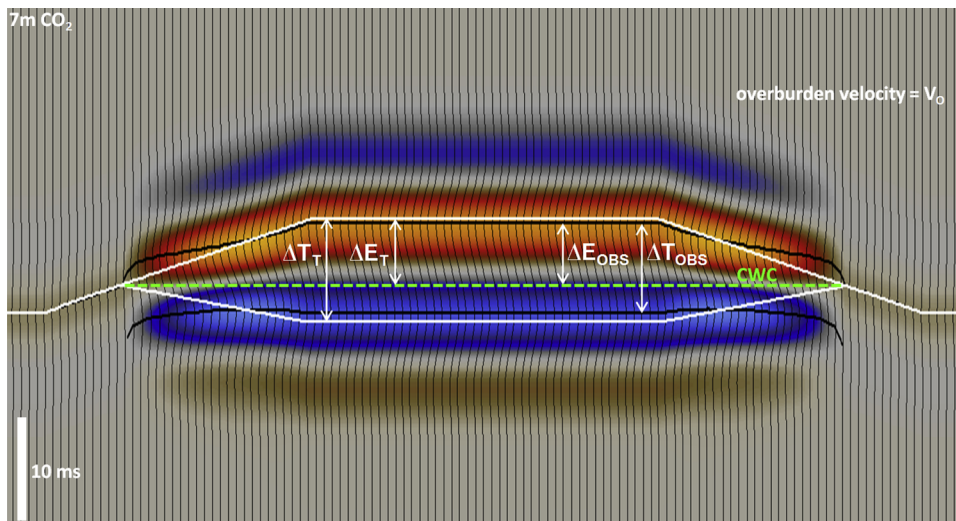

Fig. 13. Synthetic seismic two-way travel-time (TWTT) section through the ridge model where the CO_2 layer is 7 m thick. White lines show the true top and base of the CO_2 in the model. Black lines show the picked top and base of the CO_2 as imaged by the seismic. Dashed green line shows the notional position of the flat CWC with no velocity pushdown. ΔE and ΔT denote true (subscript T) and observed (subscript OBS) values of the temporal elevation of the layer top and the temporal spacing of the layer reflections.

cross-sections through the ridge model (Fig. 11) show the CO_2 as a low velocity polygon beneath the flat ridge crest. The CO_2 – water contact (CWC) is flat in the depth domain (green dashed line, Figs. 11c, e, f), but shows marked velocity pushdown on the TWTT sections displayed here. On the synthetic seismic data the CO_2 layer corresponds to enhanced reflectivity, with reflections from both the top and base of the CO_2 layer. As the layer thins towards its edges the enhanced reflectivity reduces progressively to zero where the CWC intersects the layer top. The modelling also illustrates nicely the various thin-layer interference effects alluded to above (Fig. 8). The model transect with no CO_2

(Fig. 11a, b) shows a simple weak reflection that corresponds exactly with the model velocity boundary at the top of the reservoir. A 3 m thick layer of CO_2 beneath the ridge crest (Fig. 11c, d) produces a much stronger reflection which, because the layer is below the tuning thickness, comprises an interference composite wavelet. This has a uniform sub-tuning temporal spacing of 6.1 ms and produces edge push-up, most pronounced where the layer is thinnest. A 7 m thick CO_2 layer (Fig. 11e, f) produces partial separation of the wavelet where the layer is thickest, accompanied by tuning overshoot, with the top reflection trough sitting slightly deeper than the top layer velocity interface and the base

reflection peak sitting slightly shallower than the base velocity interface. This gives an observed temporal spacing somewhat less than the true temporal spacing of the layer top and base. The ridge flanks are characterised by sub-tuning spacings and edge push-up. A 10 m thick CO_2 layer (Fig. 11g, h) produces almost fully separated reflections from the top and base of the layer where it is thickest, with observed temporal spacings close to the true temporal spacing.

It is notable that velocity pushdown beneath the ridge crest in terms of absolute travel-time is only observed beneath those parts of the ridge where the CO_2 layer is sufficiently thick (Fig. 11h), which is consistent with observations from the actual seismic data (Fig. 9b).

4.4. Extracting the velocity of the CO_2-filled layer

The basis of determining the velocity of the CO_2-filled layer is that the TWTT of the CWC is known at the layer outer edges, where the CWC intersects the layer top, independent of the layer velocity (Fig. 13). With no velocity pushdown, a notional CWC can therefore be constructed by fitting a flat horizontal surface through the TWTT of the CO_2 reflectivity limit (Fig. 13). By comparing this with the actual CWC, which is affected by velocity pushdown, the layer velocity can be obtained from the overburden velocity. To do this we define two parameters: true temporal elevation (ΔE_T) is the temporal elevation of the CO_2 layer top in the model above the notional CWC (Fig. 13) and true temporal layer spacing (ΔT_T) is the temporal elevation of the CO_2 layer top in the model above the layer base in the model (Fig. 13). The absolute thickness (in depth) of the CO_2 layer can be obtained from ΔE_T and the overburden velocity (Eq. (1)) and the layer velocity obtained by combining this with ΔT_T (Eq. (2)).

$$\text{Absolute thickness of } CO_2 \text{ layer} = \Delta E_T * V_O /2 \qquad (1)$$

And so:

$$CO_2 \text{ layer velocity } V_L = \text{Absolute thickness of } CO_2 \text{ layer} / (\Delta T_T/2)$$

$$V_L = \Delta E_T * V_O / \Delta T_T \qquad (2)$$

where V_o = velocity of the overburden

The $\Delta E / \Delta T$ parameter essentially reflects the amount of velocity pushdown within the layer. So for example a $\Delta E_T / \Delta T_T$ value equal to one would correspond to zero pushdown and a layer velocity equal to that of the overburden (V_o).

Because the synthetic model geometry and properties are known, we could extract ΔE_T and ΔT_T directly from the model and obtain an exact layer velocity from the equations above. In practice we wish to determine the velocity using observed measurements from the synthetic seismic (ΔE_{OBS} and ΔT_{OBS}). Because of the interference-induced time-shifts discussed above this would lead to a somewhat inaccurate velocity determination. Corrections therefore need to be applied to the observed seismic measurements to obtain the true values.

Two corrections are necessary, both arising from tuning overshoot (Fig. 8). First we have to correct for the fact that the observed temporal spacing ΔT_{OBS} is less than the true temporal spacing ΔT_T and second for the fact that the observed temporal elevation of the layer top ΔE_{OBS} is slightly less than the true temporal elevation ΔE_T :

$$\Delta T_T = \Delta T_{OBS} + \text{correction 1} \qquad (3)$$

$$\Delta E_T = \Delta E_{OBS} + \text{correction 2} \qquad (4)$$

The required corrections are readily extracted from the synthetic modelling datasets by comparing exact travel-times at the velocity interfaces in the velocity model with travel-times of the picks made on the corresponding seismic reflections (Fig. 14). The plots show significant scatter, because of travel-time jitter arising principally from discretisation effects on dipping interfaces in the synthetic model, but a large number of seismic traces were incorporated into the analysis

which enabled polynomial correction curves to be fitted to the data. The temporal spacing correction (Fig. 14a, b) can be plotted as a function of ΔT_{OBS} and is negative below the tuning thickness (6.8 ms) which marks the zero-crossover. The temporal elevation correction (Fig. 14c) can be plotted as a function of ΔE_{OBS} and is negative for a thin layer where edge-push-up predominates, with the zero-crossover at 4.5 ms.

It is notable that even on the noise-free synthetic seismic data the picked horizons still exhibit significant jitter due to discretisation artefacts in the model and the synthetic seismic wavelet. However, the several hundred seismic traces in the model allow measurements to be made on multiple traces with statistical treatment of the results.

Velocity analysis was carried out on a trace-by-trace basis, albeit restricted to the thicker parts of the layer, above the tuning thickness (> 6.8 ms) where the layer reflection is partially separated, and where model and measurement 'jitter' is minimised relative to the magnitude of the parameters. ΔT_{OBS} and ΔE_{OBS} were measured on a total of 649 traces, and then corrected via the respective polynomial correction functions (Fig. 14b, c) to obtain ΔT_T and ΔE_T. Layer velocity was then calculated via Eq. (2).

Results (Fig. 15) demonstrate the efficacy of the velocity extraction methodology. Corrected measurements from all traces above the tuning thickness (Fig. 15a) yield a fairly tight velocity histogram centred on 1396 ms^{-1} with a standard deviation of $\pm$ 18 ms^{-1}. Note that the velocity spread is due entirely to travel-time jitter, the actual model velocity being exactly 1400 ms^{-1}. The relative effect of travel-time jitter should be reduced at greater CO_2 layer thicknesses, and this is borne out by further restricting the analysis to traces where $\Delta T_T > 10$ ms. This reduces the number of traces to 248, but the improvement in velocity determination is quite marked (Fig. 15b), extracted velocities centring on 1399 ms^{-1} with a standard deviation of only $\pm$ 12 ms^{-1}. Velocities extracted without applying the temporal spacing and temporal elevation corrections (Fig. 15c) show much lower accuracy, averaging around 1460 ms^{-1} with a standard deviation of $\pm$ 30 ms^{-1}. The uncorrected velocities are systematically too high because the main controlling parameter is the underestimation of temporal spacing on the observed data (Fig. 13). Temporal elevations are also underestimated on the observed data which would tend to decrease extracted velocities, but this effect is outweighed by the larger error on temporal spacing.

It is important to note that extracted velocities scale directly with the overburden velocity which, for the synthetic model, is known exactly. This is not the case for the real situation (see below) and extracted velocities will carry correspondingly more uncertainty.

5. Velocity mapping in the topmost CO_2 layer of the Sleipner plume

5.1. Mapping layer temporal spacings and the CO_2 – water contact

In this section we follow the same methodology developed from the synthetic seismic modelling to extract velocities from real reflections from the topmost CO_2 layer at Sleipner. Comparison of the synthetic seismics with the real data shows striking similarities (Fig. 16), and because the position of the CWC is known exactly on the synthetic data the characteristic seismic signature of its edge cut-offs can be used to constrain mapping of the CWC on the real data. Analysis of the CWC was restricted to an area covering the central part of the plume where clear edge cut-offs and well-defined topseal topography allowed it to be constructed with a fair degree of confidence.

The reflection trough from the top of the CO_2 layer and the reflection peak from the layer base were carefully picked (Fig. 16b,c) and the CWC constructed by interpolating a smooth, flat or near-flat surface along west-east seismic lines between the edge cut-offs (Fig. 16b,c). Maps of these features (Fig. 17a,b,c) show the north-trending ridges at the layer top (Fig. 17a), underlain locally by velocity pushdown at the layer base (Fig. 17b). The CWC map shows a smooth near-flat surface
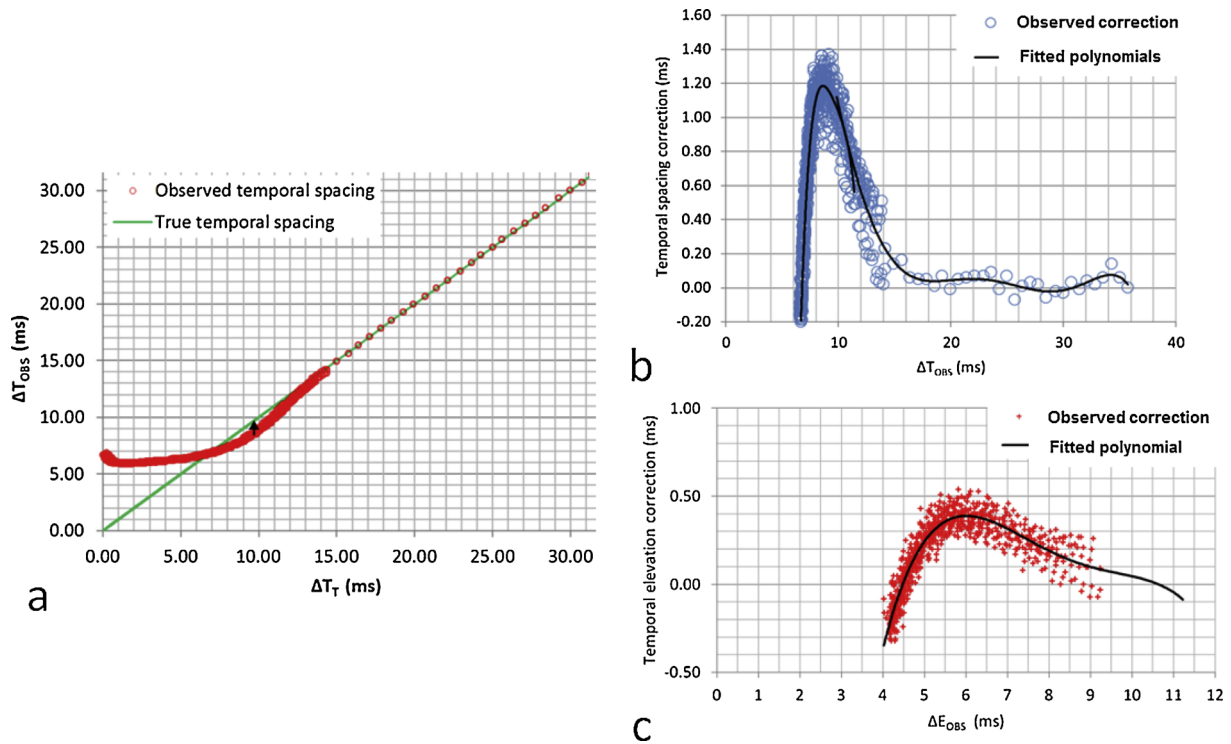
Fig. 14. a) Observed temporal spacing as a function of true temporal spacing. Small arrow indicates the necessary correction. b) Correction for observed temporal spacing derived from (a). c) Correction for observed temporal elevation. Solid lines denote polynomial functions used to apply the corrections; two overlapping functions being used in (b).

albeit with minor line-to-line variability (Fig. 17c). It is noted that minor lateral velocity variation in the overburden can cause the eastern and western cut-offs to have slightly different absolute travel-times which results in apparent tilting of the CWC. Also, where the layer is thin and spilling into complex topseal topography, dynamic flow effects can result in some parts of the CWC being not exactly horizontal. These effects are of very minor significance, particularly away from the edge limits, where the layer is thick and the velocity analysis is focused.

From these measurements the temporal spacing of the layer (ΔT_{OBS}) was calculated and also the temporal elevation of the layer top reflection above the CWC (ΔE_{OBS}). Temporal correction functions developed from the synthetic modelling (Fig. 14) were then applied to obtain the true values of these parameters ΔT_T and ΔE_T (Fig. 17d,e). These functions were based on the synthetic ridge model with *a priori* assigned layer and overburden velocities of $1400 \, ms^{-1}$ and $2150 \, ms^{-1}$ respectively. This is a valid approach because the error analysis was carried out in the temporal domain, where the functions are insensitive to model velocity structure and have general applicability. Analysis was

restricted to the thicker parts of the layer where the top and base reflections are partially separated (Fig. 10a), and specifically to traces with $\Delta T_T > 8$ ms, to avoid traces where the layer is close to the temporal tuning thickness (6.8 ms) and the effects of jitter become more significant. It is noted also that the main feeder chimney for this layer (Chadwick and Noy, 2010), around which the CWC might not be flat due to dynamic flow effects, lies outside the area of analysis, to the south west.

5.1.1. Overburden velocity

Overburden velocity is a key parameter in deriving the absolute thickness of the CO_2 layer from the temporal elevation and from this the layer velocity (Eqs. (1) and (2)). A number of wells in the vicinity have overburden velocity data, of which the closest are Norwegian wells 15/09–13 and 15/09–16, some 2 and 4 km to the WSW of the central part of the plume respectively. In addition, full spatial overburden velocity coverage is provided by stacking velocities from the 3D seismic processing which included 4th order polynomial fitting for optimal
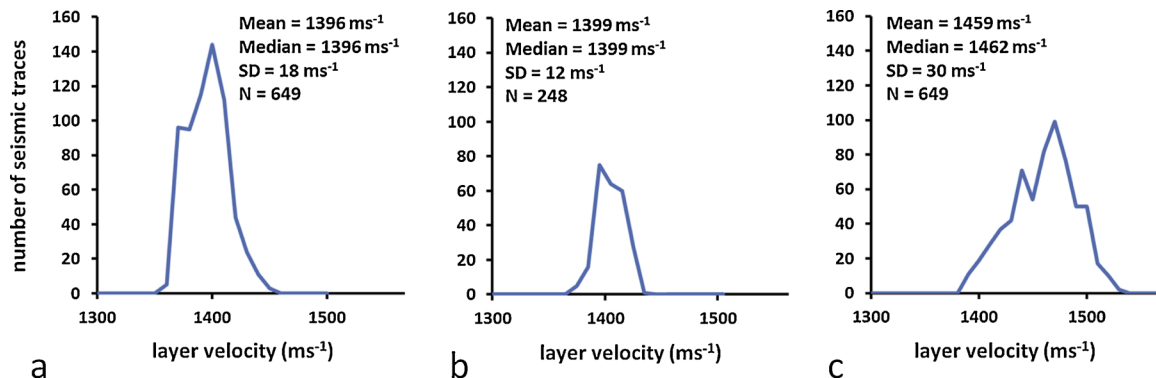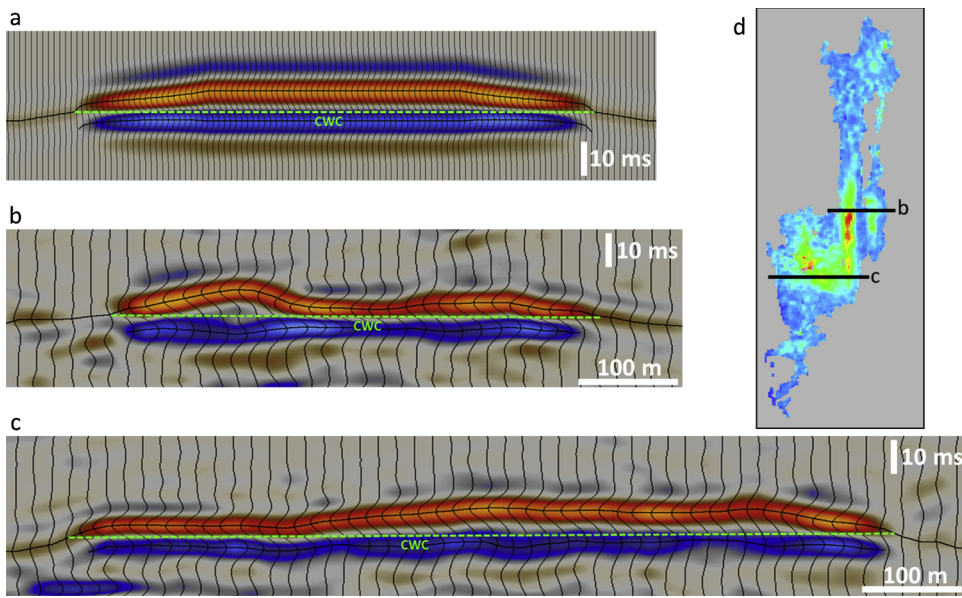

Fig. 15. Trace-by-trace velocity extractions for the synthetic CO_2 layer. a) Corrected velocities for $\Delta T_T > 6.8$ ms. b) Corrected velocities for $\Delta T_T > 10$ ms. c) Uncorrected velocities for $\Delta T_{OBS} > 6.8$ ms.

Fig. 16. Reflections from the top and base of a CO_2 layer and construction of the CWC. a) Synthetic seismic from the ridge model with known CWC. b) Observed seismic section (near-offset 2010 data) through the topmost CO_2 layer in the northern plume with constructed CWC. c) Observed seismic section (near-offset 2010 data) across the central plume with constructed CWC. d) Reflectivity map of the topmost layer with location of the two seismic sections.
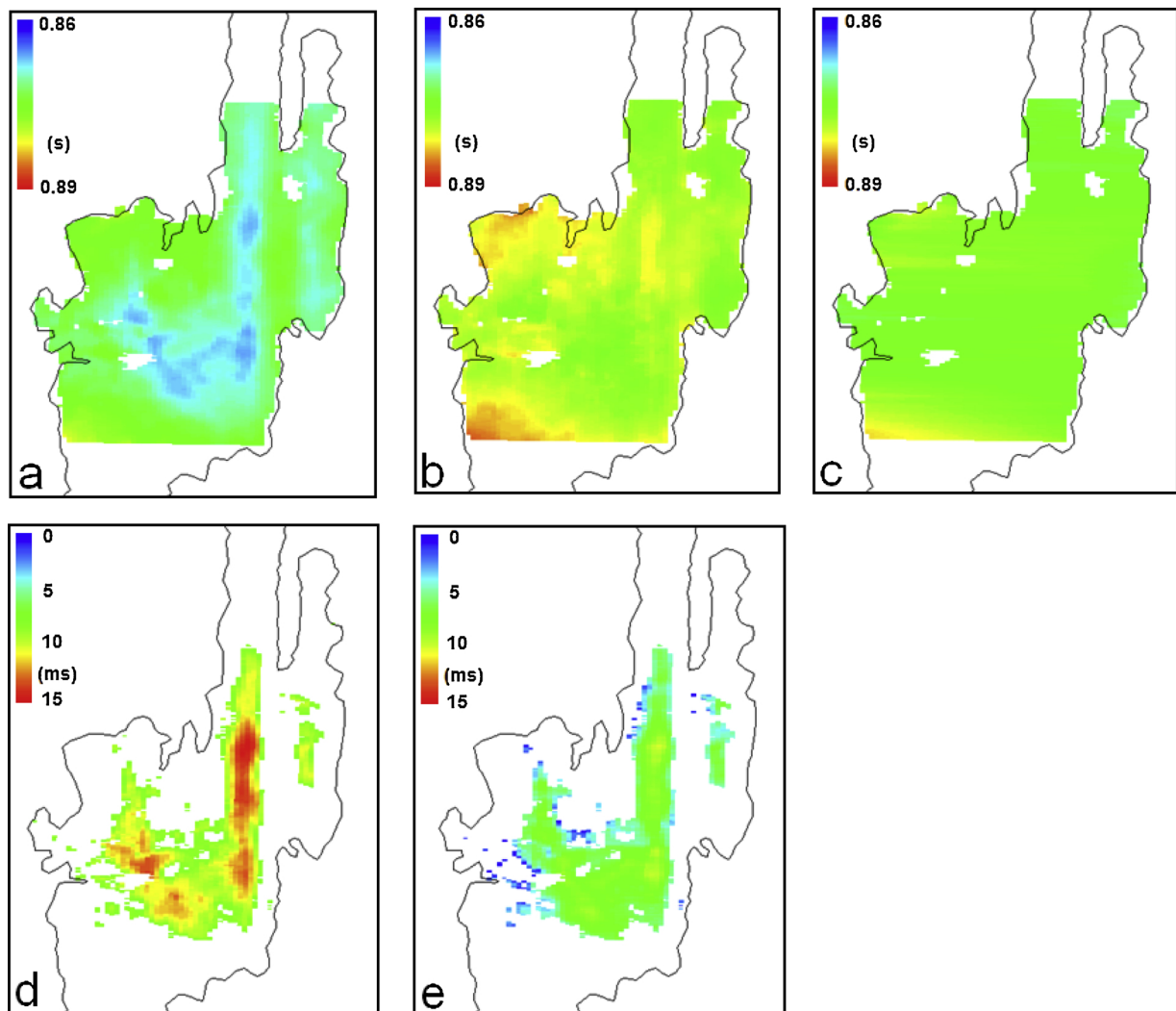
Fig. 17. Maps of the topmost CO_2 layer in 2010. a) TWTT to layer top. b) TWTT to layer base. c) TWTT to constructed CWC. d) Corrected layer temporal thickness (ΔT_T). e) Corrected temporal elevation (ΔE_T). Data restricted in (d) and (e) to traces with $\Delta T_T > 8$ ms. Polygon denotes the CWC limit of the layer.

Table 2
Interval velocities for the lower part of the overburden.

Data source	Interval velocity	Uncertainty	Comments
Nearby well logs average	2150 ms^{-1}		Zweigel et al., 2004
Well 15/09-13	2159 ms^{-1}		Basal 35 m of overburden
Well 15/09-16	2133 ms^{-1}		Basal 30 m of overburden
Dix interval velocity (seismic)	2137 ms^{-1}	± 46 ms^{-1} (SD)	Basal 50 m of overburden over plume

determination of the NMO correction (Table 2).

Both wellbore and seismic data show a general increase in overburden velocity with travel-time, but no systematic lateral variation in velocity is evident from the seismic stacking velocities. Wellbore spacings are too large to map any local variation that might be present (Chadwick and Noy, 2010), so a laterally uniform but time-variant overburden velocity was assumed. The parameter of interest is the differential topographic relief of the top reservoir surface, rather than its absolute depth, and so we place the travel-time topography at the base of a layer-cake model whose lowest layer (immediately overlying the topseal relief) has a laterally uniform constant velocity corresponding to the deepest interval of the time-variant velocity trend. This is the computational equivalent of depth-converting with a laterally uniform time-variant average velocity, but is a more convenient approach which allows analysis to be carried out in the travel-time domain with a single velocity depth conversion afterwards. In practice we calculated interval velocities for the deepest few tens of metres of the overburden (Table 2). This lies within 'Lower Seal' (Chadwick et al., 2004) which seismo-stratigraphically is rather uniform and whose interval velocity might be expected to be similarly uniform. Calculated well log values are in the range 2133 to 2159 ms^{-1}. Interpolated Dix interval velocities derived from the stacking velocities show a smooth somewhat skewed distribution with 90% of values lying in the range 2075 to 2225 ms^{-1}. Taking all this information together, a velocity value of 2150 ± 46 ms^{-1} was assigned to the basal overburden interval (V_O in Eqs. (1) and (2)).

5.2. Extracting layer velocities

Values of ΔT_T and ΔE_T were obtained for a total of 2767 seismic traces (Fig. 17d,e), corresponding generally to the central parts of the layer where temporal spacings are largest, and layer velocities were then calculated from Eq. (2). Velocities show considerable variation, ranging from around 1200 ms^{-1} to 1800 ms^{-1} (Fig. 18a). A histogram of the velocity distribution (Fig. 18b) shows a wide spread of velocities, markedly skewed, with significantly different median and mean values and a very high standard deviation (± 373 ms^{-1}). The velocity spread

reflects both real velocity variation in the layer and also the random effects of travel-time jitter. The latter will be more pronounced than on the synthetic data due to the presence of seismic noise and it is likely that jitter is producing a significant component of the observed velocity spread, actual layer velocities falling within a significantly narrower range.

The comparable histogram of the (admittedly less noisy) synthetic velocities extracted from the ridge model, which has a single exact layer velocity, shows a symmetrical distribution (Fig. 15a), with identical median and mean values and a very much smaller standard deviation (± 18 ms^{-1}). It is likely therefore that the observed skewed velocity distribution does not reflect a single layer velocity but is more consistent with a bimodal velocity distribution, with two distinct velocity means/medians of around 1400 and 1600 ms^{-1} (shown schematically in Fig. 18c). This bimodality is also consistent with the way that velocities are distributed spatially, low layer velocities within the topseal ridges to the north of the analysed area contrasting distinctly with much higher velocities in the central parts (Fig. 18a).

In order to investigate this spatial variation in more detail we selected two distinct spatial subsets from the data (Fig. 19a). A Northern Area corresponds to the north-trending ridge in the topseal (Fig. 10) and contains mostly low velocity seismic traces and a Central Area contains generally higher velocity traces. A minor zone of overlap comprises traces of intermediate velocity.

Histograms emphasise the difference in the layer velocity characteristics of the two spatial subsets (Fig. 19b). Both have quite symmetrical distributions but the Northern Area has a mean velocity of 1371 ms^{-1}, whereas the Central Area has a mean of 1638 ms^{-1}. The standard deviation in both subsets is just over ± 100 ms^{-1}, less than one third of the standard deviation for the whole dataset (Fig. 18b). Standard deviations for the two subsets are larger than for the synthetic data, but this is to be expected because the observed data is noisier than the synthetics and also there is very likely a real variability in layer velocity within each area, as opposed to the single value in the synthetic model. Overall therefore, the distributions strongly support two distinct velocity populations.

The velocity contrast is manifest in the way that the layer is imaged in
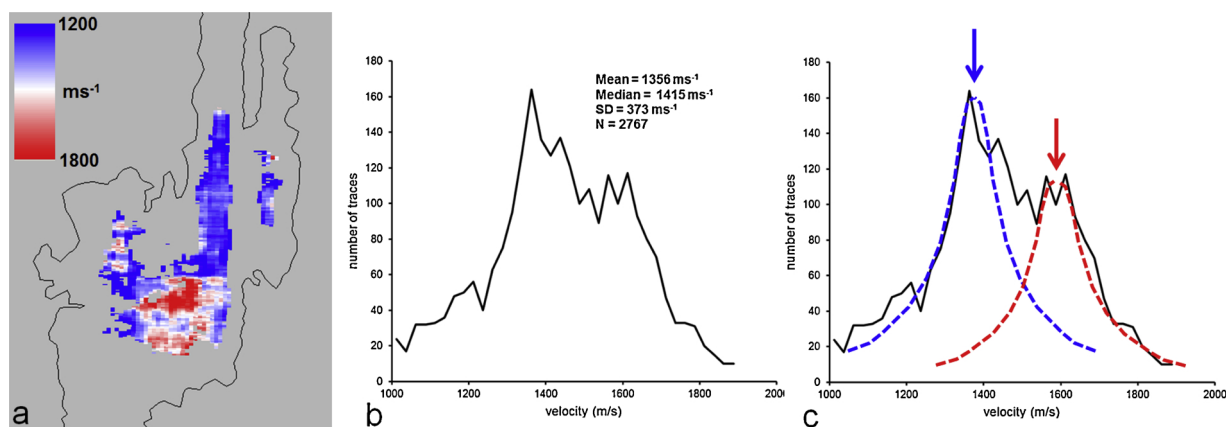
Fig. 18. Velocity analysis for the topmost CO_2 layer for traces with $\Delta T_T > 8$ ms. a) Extracted velocities. b) Histogram of velocity variation. c) As for (b) but with two distinct schematic normal distribution curves superimposed. Arrows denote median values of the schematic curves. Polygon in (a) denotes the CWC limit of the topmost layer in 2010.
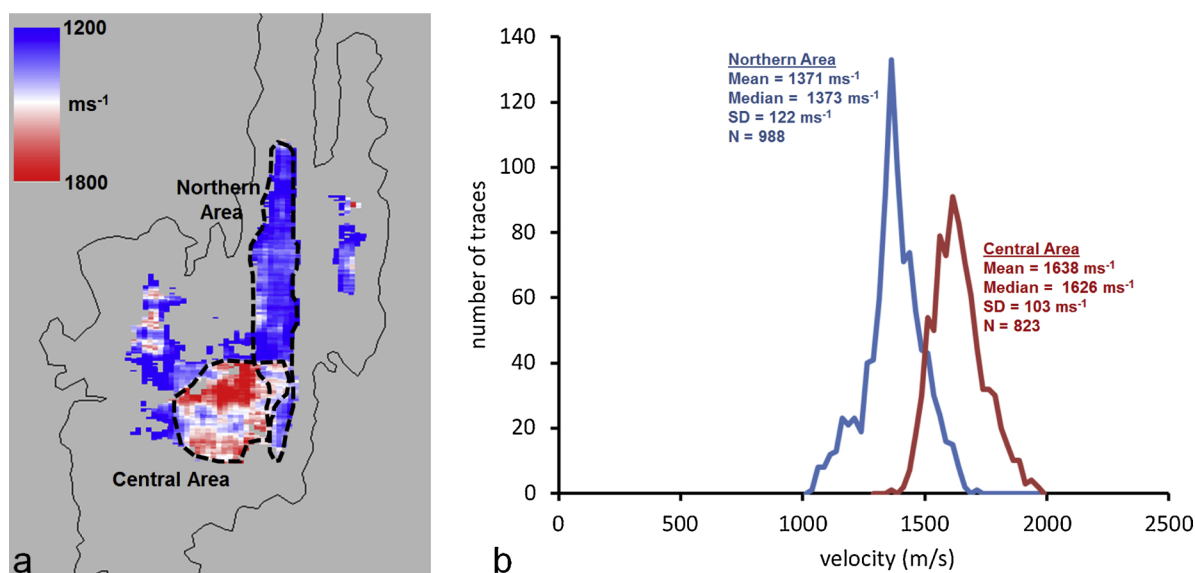
Fig. 19. Velocity analysis for two selected areas in the topmost CO_2 layer for traces with $\Delta T_T > 8$ ms. a) Extracted velocities with areas marked. b) Velocity histograms for the two areas.

the two areas. Seismic data in the Northern Area (Fig. 16b), in the partially separated domain, typically show the constructed CWC lying around 60% of the way down from the top layer reflection to the base layer reflection ($\Delta E / \Delta T \sim 0.6$), whereas in the Southern Area (Fig. 16c) the constructed CWC typically lies around 70–80% of the way towards the base layer reflection ($\Delta E / \Delta T \sim 0.7$-0.8). This is because, for similar layer thicknesses, velocity pushdown of the base layer reflection is less severe in the Central Area than in the Northern Area, in accordance with the higher layer velocity.

5.2.1. Uncertainty and errors

It is important to examine the various sources of error and uncertainty in the velocity analysis and judge whether these could reasonably give rise to the observed lateral velocity variation. Errors in the velocity determination stem from three main types of uncertainty – the accuracy with which the notional CWC can be positioned from the seismic data, the impact of overburden velocity variation on the mapping of topseal topography, and possible spatial instability of the seismic wavelet.

5.2.1.1. Position of the CO_2-water contact (CWC). Positioning and construction of the notional CWC is a rather qualitative interpretive issue, but assessment of line-to-line variation on the CWC two-way travel-time indicates a maximum mismatch between adjacent lines of 1 ms, and generally significantly less than this. A positioning error of ± 1 ms on the CWC would translate to a velocity error of around ± 180 ms^{-1} where the layer is thick, which corresponds roughly to the extreme limits of the velocity histograms (Fig. 19). This is an essentially random effect that contributes to the calculated velocity scatter, but does not change the central velocity values (as shown by the statistical analysis of the synthetic data presented above). It is important also to stress that the image characteristics of the CWC termination at the layer edge do remain consistent across the interpreted area (Fig. 16), with no systematic spatial variation that might change the way in which the CWC was positioned at the CO_2 layer edge across the area.

Temporal 'jitter' on the top and base layer seismic picks due to seismic noise is another random effect that contributes to the observed velocity scatter but would not affect the central velocity determination.

A potential systematic error in positioning the CWC is related to the method of constructing it horizontally from the edge cut-offs of the CO_2 layer. Because of capillary effects the base of a real CO_2 layer would not

project exactly horizontally from the edge cut-off, but would actually warp downwards slightly, adding a small additional thickness to the layer. This will slightly increase ΔT whilst ΔE remains unchanged; the overall effect being to reduce calculated layer velocities slightly compared with the true velocity. Comparison of analytical and high-resolution numerical flow models by Williams et al. (2018) suggests that the capillary fringe at Sleipner is only about 0.5 m, so the effect would be very small particularly as the base layer reflection peak would be smeared somewhat across the CO_2 saturation gradient in the fringe. The velocity reduction artefact should be more pronounced where the layer is thin, so to test for evidence of this we examined velocities extracted from two layer thickness ranges, one with ΔT_T in the range 8–10/11 ms and one with ΔT_T from $> 10/11$ ms upwards (Fig. 20).

Northern Area velocities extracted from the thinner parts of the layer are somewhat lower than velocities from the thicker parts (Fig. 20a). This is what would be expected from the velocity artefact, but the difference is probably not statistically significant. Central Area velocities extracted from the thinner parts of the layer are however higher than velocities from the thicker parts (Fig. 20b), opposite to what would be expected from the velocity artefact. It seems therefore that a slightly mis-positioned CWC has a limited effect on extracted velocities.

What is clear from this analysis is the fact that restricting velocity determinations to just the thickest parts of the layer ($\Delta T_T > 10$ or 11 ms) does significantly reduce the spread or scatter in extracted values and might well give the most accurate overall velocity determination for the two areas.

5.2.1.2. Overburden velocity variation. A second potential source of error lies in the velocity structure of the overburden which affects the fidelity with which the topseal topography is imaged. Layer velocities scale directly with the velocity of the lowermost overburden layer immediately overlying the topseal relief (Eq. (2)). On the scale of the features analysed this has an estimated uncertainty of around ± 2% (see above) so absolute calculated layer velocities will be subject to a similar uncertainty. This range is nearly an order of magnitude smaller than the calculated spatial variation in layer velocity which approaches 20%.

In terms of lateral velocity changes, local variation in the overburden immediately overlying the CO_2 plume cannot be ruled out, but maps of interpolated interval velocity derived from the stacking velocities show no sign of a systematic lateral velocity pattern that could
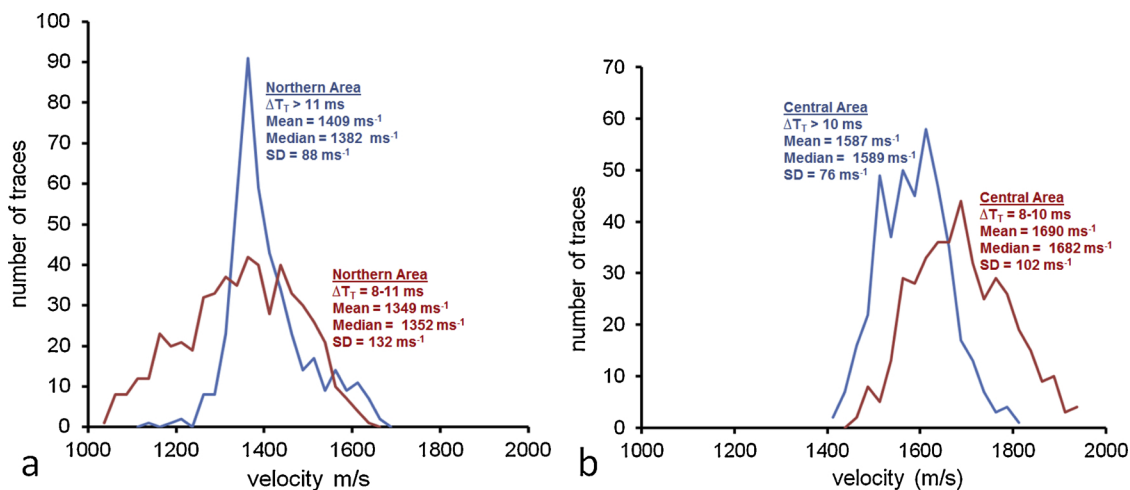
Fig. 20. Variation of extracted velocity with temporal thickness (ΔT_T) of the layer. a) Northern Area. b) Central Area. N.B. ΔT_T sample ranges were chosen to have roughly equal numbers of traces in each.

distort the layer velocity analysis. A broader, monotonic velocity 'slope' across the area can be discounted, because if it were present then the assumption of constant depth-conversion velocity would impose a false tilt on the topseal topography. This would have the effect of significantly altering the shape of the layer (Chadwick and Noy, 2010), whereas recent flow simulations using topography from a laterally uniform depth-conversion velocity (e.g. Cowton et al., 2018) show strikingly good agreement with the observed layer footprint.

More localised lateral velocity variation in the shallower overburden could give rise to local temporal distortion of the top layer reflection. The formation most likely to produce this is a so-called 'gassy layer' a zone within the overburden at a depth of around 600 m characterised by seismic bright-spots attributed to the presence of natural gas (Arts et al., 2004a, 2004b). In order to assess this we mapped total reflectivity in the gassy layer to see if this correlated in any way with the calculated velocities (Fig. 21). In fact there is very little overall variation in the gassy layer above much of the analysed area and no correlation at all with the marked velocity step between the Northern and Central areas (Fig. 21a, b). It is notable though that farther west some stronger bright-spots are present. One of these (Fig. 21c) overlies the analysed area in the far west and does cast a 'shadow' on the CO_2

layer producing a significant local velocity pushdown (Fig. 21c). The effect of this is to decrease the $\Delta E / \Delta T$ ratio giving an artificially slow layer velocity beneath the bright-spot (Fig. 21a), with the implication that true slow layer velocities might be mostly restricted to the Northern Area and the ridge farther to the east.

Uncertainties regarding the velocity analysis seem therefore to be as follows: systematic effects that might affect absolute velocity values across the area but are smaller than and do not correlate with the observed spatial variation; local effects that do not correlate with the observed spatial variation; and small random errors, again that do not correlate spatially with the observed variation. The interpreted lateral velocity change from the Northern Area to the Central Area is therefore deemed to be robust.

5.2.1.3. Spatial variation of the seismic wavelet. A final potential source of error is the extent to which the seismic wavelet is spatially stable across the area. If the wavelet were to change laterally, and in a systematic way, then that could produce an artificial contribution to the layer velocity variation. To test this, wavelets were analysed for the two velocity areas (Fig. 22).

This requires a different approach from that used to determine the
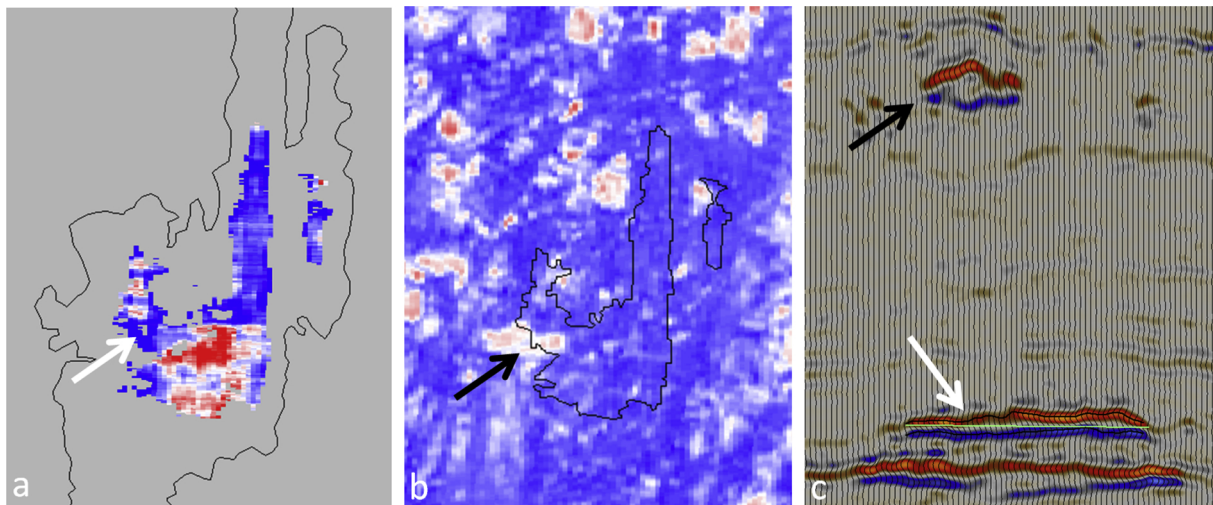

Fig. 21. a) Northern and Central areas velocities (red = high, blue = low). Polygon denotes limit of the topmost CO_2 layer. b) RMS amplitudes (red = high, blue = low) from the overburden gassy layer. Polygon denotes footprint of the Northern and Central areas. c) Seismic line (near-offsets) showing bright-spot in the gassy layer and underlying velocity pushdown of the CO_2 layer reflections. Black arrows denote the position of the bright-spot, white arrows the impact on the CO_2 layer reflectivity and extracted velocity.
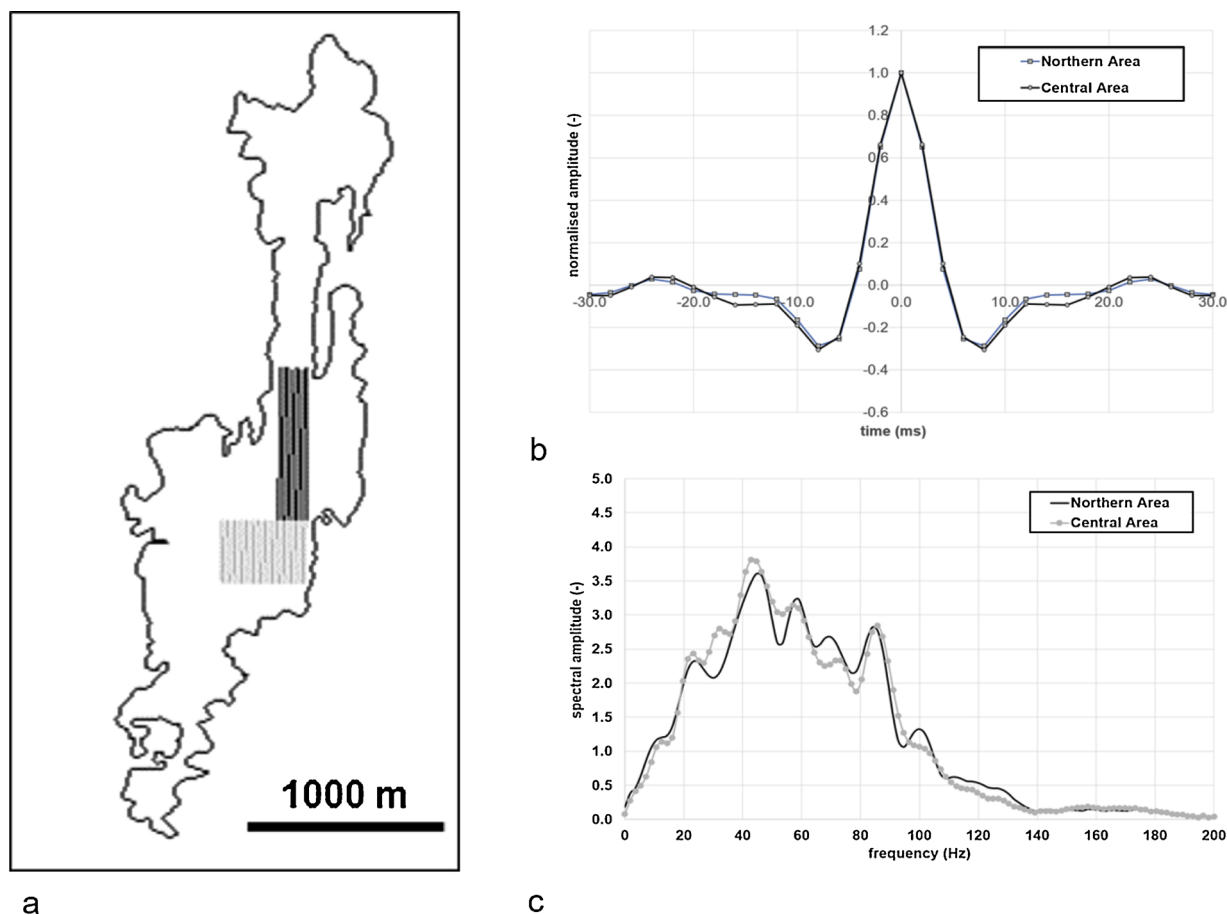
Fig. 22. Wavelet extraction from the Northern and Central velocity areas. a) Shaded rectangles denote traces used in analysis. b) Extracted wavelets. c) Frequency spectra.

seismic wavelet in the synthetic modelling, which focussed on the topmost Utsira Sand, but well away from the reflective CO_2 plume to avoid its strong tuning effects (see above). Here it is necessary to analyse wavelets from directly above the topmost CO_2 layer; but to avoid the strong tuned plume reflections, analysis was restricted to the overburden. This would reveal any systematic overburden attenuation variation that might affect the downgoing wavelet. Seismic traces were extracted from a window between 256 and 756 ms TWTT, in two rectangular areas overlying the Northern and Central velocity areas, containing 968 and 1173 traces respectively (Fig. 22a). Extracted wavelets from the two areas are very similar in terms of their shape, notably the peak-to-side-lobe spacings and relative amplitudes (Fig. 22b), and also in their spectral content (Fig. 22c). It is concluded therefore that wavelet variability does not make any significant contribution to the observed layer velocity variation.

5.3. Reflectivity changes in topmost layer

The proposed variation in seismic velocity in the topmost layer should also be marked by a significant change in layer reflectivity. However local lithological variation in the overlying topseal, local attenuation effects from the overburden, strong tuning effects and other forms of seismic noise can all act to make amplitudes rather unpredictable. In principle time-lapse difference data should give the best indication of reflectivity variation, as the effects of baseline variations in reservoir reflectivity are largely removed. A time-lapse version of the 2010 data is available, matched to the 1994 baseline survey. Time-lapse processing of the 2010 data markedly reduces the bandwidth of the seismic wavelet, so tuning effects are more pronounced at higher

temporal spacings than on the full resolution survey and it is not straightforward to quantitatively assess the variation in reflection amplitudes. Suffice to say here that the time-lapse difference data (Fig. 23) do show systematically higher RMS reflection amplitudes over the Northern Area compared to the Central, which is consistent with lower seismic velocities in the former.

6. Discussion

6.1. Velocities and channelling

Rock physics using the natural range of sand properties observed from Utsira Sand well logs indicates that the velocities of CO_2 layers could range from < 1400 to > 1500 ms^{-1} for high CO_2 saturations, with higher velocities at intermediate CO_2 saturations (Fig. 7), the latter supported by recent experimental data and calibrated rock physics from the Utsira core (Falcon-Suarez et al., 2018). This suggests that observed spatial variation in the topmost CO_2 layer velocity, from around 1370 ± 120 ms^{-1} in the Northern Area to around 1630 ± 103 ms^{-1} in the Central Area, can be explained by spatial variation in reservoir sand properties (Fig. 7).

Thus, low layer velocities correspond to higher CO_2 saturations in more porous 'slow' sand whereas higher layer velocities correspond to perhaps intermediate CO_2 saturations in lower porosity 'fast' sand.

This is supported by baseline seismic data from the reservoir (Fig. 24). Isochores of the topmost sand unit show prominent north-trending linear zones of thickening, interpreted as channels, with temporal thicknesses around 30 ms (Fig. 24b). Away from the channels temporal sand thicknesses are lower, generally in the range 15–25 ms,
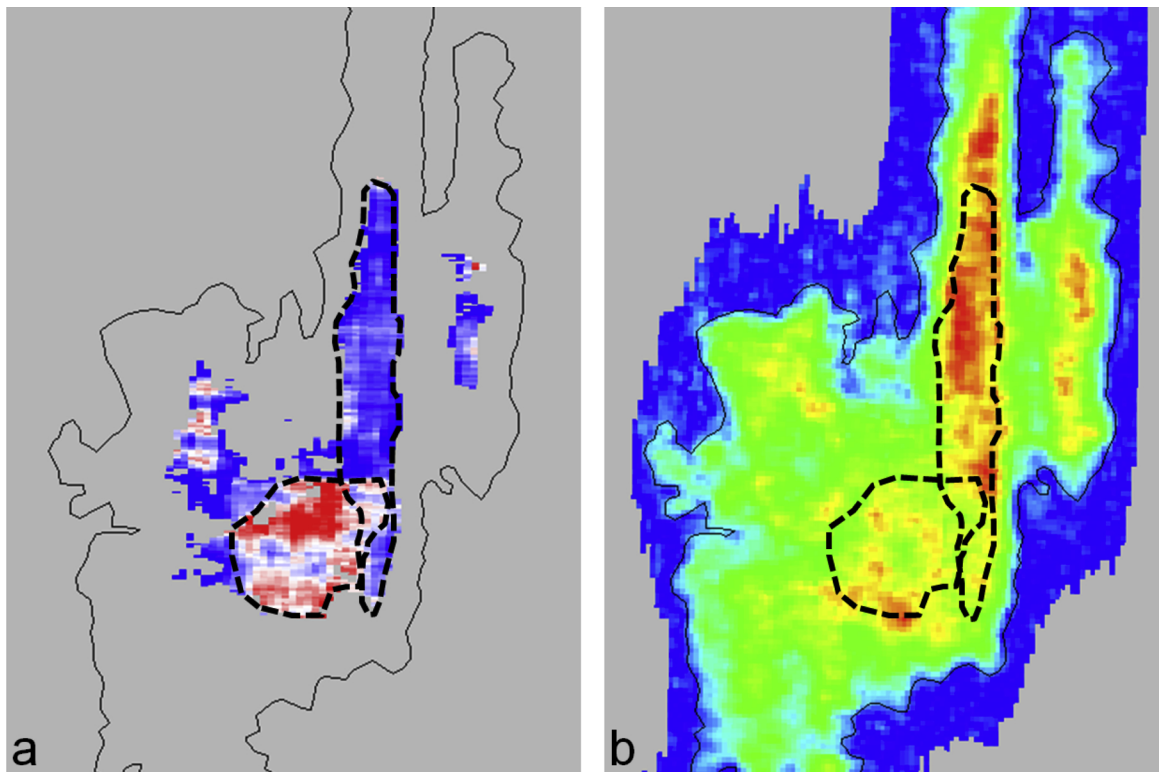
Fig. 23. a) Northern and central areas velocities (red = high, blue = low). b) RMS reflection amplitudes on the top reservoir interface from the 2010 – 1994 time-lapse difference data. Faint polygon denotes limit of the topmost CO_2 layer.

and are interpreted as platformal or inter-channel areas. In general, the sedimentary fill of the channels would be expected to be of a thicker-bedded and coarser-grained sedimentary facies than the platformal areas. This is consistent with the findings of Cowton et al. (2018) who used spectral decomposition on the baseline seismic data to identify areas of lower seismic frequency corresponding to the channels, and suggestive of thicker bed-forms than elsewhere.

The correlation of the western channel with the Northern Area low layer velocity feature is particularly striking (Fig. 24a,c) with a smaller extracted area of low velocities to the east corresponding to the eastern channel. The Central Area of higher velocities is interpreted to lie

within a more platformal or inter-channel setting. It is notable that the Utsira core was obtained from well 15/9-A23, which lies in an intermediate position between the main channels and the elevated inter-channel areas (Williams and Chadwick, 2017). Core velocities, at least for the higher experimentally determined CO_2 saturations, lie roughly between those of the Central Area and Northern Area, consistent with this intermediate position (Fig. 7).

6.2. Permeability heterogeneity

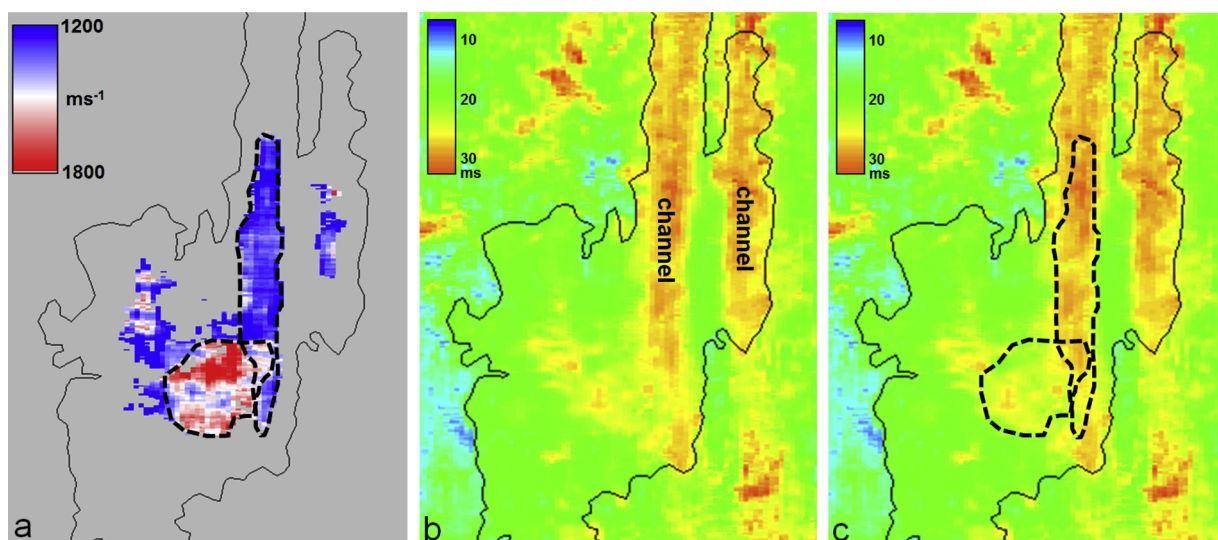Given that sand permeability generally increases with both porosity

Fig. 24. a) Extracted velocities and location of Northern and Central areas. b) Isochore map of the topmost sand unit in 1994 showing prominent north-trending channels. c) as for (b) but with locations of Northern and Central areas superimposed. Faint black polygon shows outline of topmost CO_2 layer in 2010.

and grain size (e.g. Kozeny, 1927; Beard and Weyl, 1973), it is likely that the channel features identified from the baseline seismic data and characterised by lower seismic velocities when saturated with CO_2, are also characterised by higher permeability.

Core samples from the Utsira show an unconsolidated moderately to well-sorted sand, with a volumetric model grain size of around 0.2 mm (Zweigel et al., 2004). Under the grainsize-sorting criteria of Beard and Weyl (1973) this suggests permeabilities in the range 5–20 Darcy. These are fully in accordance with the permeability values that Williams and Chadwick (2017) and Cowton et al. (2018) use to history-match the topmost layer with the channelled reservoir flow models.

History-matching of the topmost CO_2 layer using Darcy-based flow simulators has proved challenging (e.g. Chadwick and Noy, 2010; Zhu et al., 2015). In particular the very rapid northward migration of CO_2 along the relatively level north-trending ridge from 2001 to 2010 (Fig. 4a), at rates averaging about 0.5 m per day (Fig. 3b), has proved difficult to replicate. Because flow in the topmost layer is dominated by buoyancy, rather than pressure-driven viscous forces, some authors (e.g. Cavanagh, 2013; Cavanagh and Haszeldine, 2014) have suggested that Darcy-based flow models might not be wholly appropriate, and so flow simulators incorporating alternative physics have been proposed, notably the invasion-percolation (IP) scheme (Cavanagh, 2013). In fact, until recently the Darcy-based flow simulations all assumed essentially homogeneous reservoir properties, albeit incorporating some elements of anisotropy. But recent publications (Williams and Chadwick, 2017; Cowton et al., 2018) have incorporated an explicit high permeability depositional channel into the flow model reservoir. This greatly improves the ease of obtaining a good history-match, with the implication that incorporating additional geological detail removes the need for alternative physics in the flow simulator.

7. Conclusions

A key objective of the time-lapse 3D seismic monitoring programme at Sleipner is to quantitatively verify or constrain predictive flow simulations of plume development to demonstrate understanding of reservoir processes and provide the basis for predicting future plume behaviour. Seismic velocity is a key diagnostic of CO_2 layer properties but deriving velocities directly from seismic data has proved very challenging at Sleipner due to the very thin layers, associated strong tuning effects, and lack of borehole calibration.

Here we adopted a forensic interpretative approach to determine spatial velocity variation in the topmost CO_2 layer. Velocity was obtained trace-by-trace, by equating absolute layer thickness, derived by subtracting a constructed flat CO_2 – water contact from the topographical relief of the reservoir top, to the temporal spacing of the layer top and base reflections. The method relies on measuring very small time-shifts, with appropriate corrections for reflection interference effects and was tested on a synthetic model with known layer velocity, producing satisfactory results. Layer velocities calculated from the 2010 seismic dataset range from around $1200 \, \text{ms}^{-1}$ to $1800 \, \text{ms}^{-1}$. The extreme limits of this range are due to the effects of seismic noise and minor interpretive uncertainties which cause travel-time jitter; a narrower but nevertheless significant velocity range is consistent with predictions from rock physics and also with recent experimental measurements from Utsira core. This rather wide range of velocities is associated with a systematic spatial difference between a Northern Area with slow layer velocities and a Central Area with much faster velocities. Velocity histograms of both areas show normal distributions with mean/median velocity values of around 1372 and $1632 \, \text{ms}^{-1}$ for the Northern and Southern areas respectively. Uncertainties relate principally to overburden velocity variations, but systematic examination and assessment of these effects indicates that the interpreted spatial variation in layer velocity is robust.

It is notable that a channel feature recently interpreted in the topmost sand body on the baseline seismic data correlates almost perfectly

with the low velocity sands of the Northern Area, with the higher velocity sands of the Central Area corresponding to a platform or inter-channel area. Lower velocities would be expected to be associated with higher sand porosities and, by implication, higher permeabilities. This does appear to be the case, because including the channel as a high permeability feature in recent fluid flow models of the topmost CO_2 layer greatly improves the ease of obtaining a good history-match.

We conclude therefore that the analysis presented here has enabled for the first time, mapping of important velocity heterogeneity in the Utsira Sand at Sleipner, and that this is associated with channel-related sedimentary and permeability heterogeneity.

Declaration of Competing Interest

The authors declare that they have no known competing financial interests or personal relationships that could have appeared to influence the work reported in this paper.

Acknowledgements

References

Alnes, H., Eiken, O., Nooner, S., Sasagawa, G., Stenvold, T., Zumberge, M., 2011. Results from Sleipner gravity monitoring: updated density and temperature distribution of the CO_2 plume. Energy Procedia 4, 5504–5511.

Arts, R., Eiken, O., Chadwick, R.A., Zweigel, P., Van Der Meer, L., Zinszner, B., 2004a. Monitoring of CO_2 injected at Sleipner using time-lapse seismic data. Energy 29, 1383–1393 Elsevier Science Ltd, Oxford.

Arts, R., Eiken, O., Chadwick, R.A., Zweigel, P., Meer, Van Der, Kirby, G., 2004b. Seismic monitoring at the Sleipner underground CO_2 storage site (North Sea). In: Baines, S.J., Worden, R.H. (Eds.), Geological Storage of CO_2. Geological Society, vol. 233. Special Publication, London, pp. 181–191.

Arts, R.J., Chadwick, R.A., Eiken, O., Thibeau, S., Nooner, S., 2008. Ten years' experience of monitoring CO_2 injection in the Utsira Sand at Sleipner, offshore Norway. First Break 26, 65–72.

Baklid, A., Korbøl, R., Owren, G., 1996. Sleipner Vest CO_2 Disposal, CO_2 Injection into a Shallow Underground Aquifer. SPE Paper 36600, Presented at 1996 SPE Annual Technical Conference and Exhibition. Denver Colorado, USA 6-9 October 1996.

Beard, D.C., Weyl, P.K., 1973. The influence of texture on porosity and permeability of unconsolidated sand. Bull. Am. Assoc. Petrol. Geol. 57, 349–369.

Boait, F.C., White, N.J., Bickle, M.J., Chadwick, R.A., Neufeld, J.A., Huppert, H.E., 2012. Spatial and temporal evolution of injected CO_2 at the Sleipner Field, North Sea. J. Geophys. Res. 117, B03309. https://doi.org/10.1029/2011JB008603.

Cavanagh, A., 2013. Benchmark calibration and prediction of the Sleipner CO_2 plume from 2006 to 2012. Energy Procedia 37, 3529–3545.

Cavanagh, A.J., Haszeldine, R.S., 2014. The Sleipner storage site: capillary flow modelling of a layered CO_2 plume requires fractured shale barriers within the Utsira Formation. Int. J. Greenhouse Gas Control 21, 101–112.

CCC, 2019. Net Zero Technical Report. Committee on Climate Change. . http://www.theccc.org.uk/publications.

Chadwick, R.A., Zweigel, P., Gregersen, U., Kirby, G.A., Johannessen, P.N., Holloway, S., 2004. Characterisation of a CO_2 storage site: The Utsira Sand, Sleipner, northern North Sea. Energy 29, 1371–1381 Elsevier Science Ltd, Oxford.

Chadwick, R.A., Arts, R., Eiken, O., 2005. 4D seismic quantification of a growing CO_2 plume at Sleipner, North Sea. In: Dore, A.G., Vining, B. (Eds.), Petroleum Geology: North West Europe and Global Perspectives - Proceedings of the 6th Petroleum Geology Conference. Petroleum Geology Conferences Ltd. Published by the Geological Society, London 1385 – 1399.

Chadwick, R.A., Noy, D.J., 2010. History – matching flow simulations and time-lapse seismic data from the Sleipner CO_2 plume. In: Vining, B.A., Pickering, S.C. (Eds.), Petroleum Geology: From Mature Basins to New Frontiers - Proceedings of the 7th Petroleum Geology Conference. Petroleum Geology Conferences Ltd. Published by the Geological Society, London 1171-1182.

Chadwick, R.A., Williams, G.A., Williams, J.D.O., Noy, D.J., 2012. Measuring pressure performance of a large saline aquifer during industrial scale CO_2 injection: the Utsira Sand, Norwegian North Sea. Int. J. Greenhouse Gas Control 10, 374–388.

Chadwick, R.A., Williams, G.A., White, J.C., 2016. High resolution imaging and characterisation of a CO_2 layer at the Sleipner CO_2 storage operation using time-lapse seismics. First Break 34, 79–87.

Clochard, V., Delépine, N., Labat, K., Ricarte, P., 2010. CO_2 plume imaging using 3D pre-

stack stratigraphic inversion: a case study on the Sleipner field. First Break 28, 91–96.

Cowton, L.R., Neufeld, J.A., White, N.J., Bickle, M.J., White, J.C., Chadwick, R.A., 2016. An inverse method for estimating thickness and volume with time of a thin CO_2-filled layer at the Sleipner Field, North Sea. Journal of Geophysical Research (Solid Earth) 121, 5068–5085.

Cowton, L.R., Neufeld, J.A., White, N.J., Bickle, M.J., Williams, G.A., White, J.C., Chadwick, R.A., 2018. Benchmarking of vertically-integrated CO_2 flow simulations at the Sleipner Field, North Sea. Earth. Planet. Sci. Lett. 491, 121–133.

Delépine, N., Clochard, V., Labat, K., Ricarte, P., 2011. Post-stack stratigraphic inversion workflow applied to carbon dioxide storage: application to the saline aquifer of Sleipner field. Geophys. Prospect. 59, 132–144.

Eiken, O., 2019. Twenty years of Monitoring CO_2 injection at Sleipner. In: Davis, T.L., Landrø, M., Wilson, M. (Eds.), Geophysics and Geosequestration. Cambridge University Press, 209-234.

Energy Technologies Institute, 2015. Options Choices Actions. UK scenarios for a low carbon energy transition system. https://www.eti.co.uk/insights/options-choices-actions-uk-scenarios-for-a-low-carbon-energy-system.

Falcon-Suarez, I., Papageorgiou, G., Chadwick, A., North, L., Best, A., Chapman, M., 2018. CO_2-brine flow-through on an Utsira Sand core sample: experimental and modelling. Implications for the Sleipner storage field. Int. J. Greenhouse Gas Control 68, 236–246.

Furre, A.-K., Eiken, O., 2014. Dual sensor streamer technology used in Sleipner CO_2 injection monitoring. Geophys. Prospect. 62 (5), 1075–1088. https://doi.org/10.1111/1365-2478.12120.

Furre, A.-K., Kiaer, A., Eiken, O., 2015. CO_2-induced seismic time shifts at Sleipner. Interpretation 3/3, SS23–SS35.

Galloway, W.E., 2002. Paleogeographic setting and depositional architecture of a sand-dominated shelf depositional system, Miocene Utsira Formation, North Sea Basin. J. Sediment. Res. 72 (4), 476–490.

Ghosh, R., Sen, M.K., Vedanti, N., 2015. Quantitative interpretation of CO_2 plume from Sleipner (North Sea), using post-stack inversion and rock physics modeling. Int. J. Greenhouse Gas Control 32, 147–158.

Gregersen, U., Michelsen, J.C., 1997. Stratigraphy and facies distribution of the Utsira Formation and the Pliocene sequences in the northern North Sea. Marine and Petroleum Geology 14 (7/8), 893–914.

IPCC, 2005. Carbon Dioxide Capture and Storage. IPCC Special Report on Carbon Dioxide Capture and Storage. Prepared by Working Group III of the Intergovernmental Panel on Climate Change. Published for the Intergovernmental Panel on Climate Change.

Cambridge University Press, New York.

Kallweit, R.S., Wood, L.C., 1982. The limits of resolution of zero-phase wavelets. Geophysics 47, 1035–1046.

Kiær, A., 2015. Fitting top seal topography and CO_2 layer thickness to time-lapse seismic amplitude maps at sleipner. Interpretation 3 (2), SM47–SM55.

Kozeny, J., 1927. Ueber kapillare Leitung des Wassers im Boden. Sitzungsber Akad. Wiss., Wien 136, 271–306.

Papageorgiou, G., Amalokwu, K., Chapman, M., 2016. Theoretical derivation of a Brie-like fluid mixing law. Geophys. Prospect. 64, 1048–1053. https://doi.org/10.1111/1365-2478.12380.

Papageorgiou, G., Chapman, M., 2017. Wave propagation in rocks saturated by two immiscible fluids. Geophys. J. Int. 209, 1761–1767 Doi:10/1093/gji/ggx128.

Queißer, M., Singh, S.C., 2013a. Full waveform inversion in the time lapse mode applied to CO_2 storage at Sleipner. Geophys. Prospect. 61 (3), 537–555.

Queißer, M., Singh, S.C., 2013b. Localizing CO_2 at Sleipner Seismic images versus P-wave velocities from waveform inversion. Geophysics 78 (3), B131–B146.

Raknes, E.B., Weibull, W., Arntsen, B., 2015. Three-dimensional elastic full waveform inversion using seismic data from the Sleipner area. Geophys. J. Int. 202 (3), 1877–1894.

White, J.C., Williams, G.A., Chadwick, R.A., Furre, A.-K., Kiaer, A., Cowton, L., 2018. Sleipner: the ongoing challenge to determine the thickness of a thin CO_2 layer. Int. J. Greenhouse Gas Control 69, 81–95.

Widess, M.B., 1973. How thin is a thin bed? Geophysics 38, 1176–1180. https://doi.org/10.1190/1.1440403.

Williams, G.A., Chadwick, R.A., 2017. An improved history-match for layer spreading within the Sleipner plume including thermal propagation effects. Energy Procedia 114, 2856–2870.

Williams, G.A., Chadwick, R.A., Vosper, H., 2018. Some thoughts on Darcy-type flow simulation for modelling underground CO_2 storage based on the Sleipner CO_2 storage operation. Int. J. Greenhouse Gas Control 68, 164–175.

Zhu, C., Zhang, G., Lu, P., Meng, I., Ji, X., 2015. Benchmark modeling of the Sleipner CO_2 plume: calibration to seismic data for the uppermost layer and model sensitivity analysis. Int. J. Greenhouse Gas Control 43, 233–246.

Zweigel, P., Arts, R., Lothe, A.E., Lindeberg, E., 2004. Reservoir geology of the Utsira Formation at the first industrial-scale underground CO_2 storage site (Sleipner area, North Sea). In: Baines, S.J., Worden, R.H. (Eds.), Geological storage of CO_2. Geological Society, vol. 233. Special Publication, London, pp. 165–180.